Article

Influence of the Arrangement of the Cells/Modules of a Traction Battery on the Spread of Fire in Case of Thermal Runaway

Ana Olona [1] and Luis Castejón [2,*]

1 Research Department, Electric Vehicle and Mobility Area, Instituto de Investigación Sobre Vehículos, S.A., Ctra. N232, km 273, 50690 Pedrola, Spain; a.olona@centro-zaragoza.com
2 Department of Mechanical Engineering, University of Zaragoza, C/María de Luna s/n, 50018 Zaragoza, Spain
* Correspondence: luiscast@unizar.es; Tel.: +34-976762556

Abstract: When designing the battery of an electric vehicle, different parameters must be considered to obtain the safest arrangement of the battery/modules/cells from the mechanical and thermal points of view. In this study, the thermal runaway propagation mechanism of lithium-ion cells is analyzed as a function of their arrangement within a battery pack in case of a fire propagation of a battery pack in which a thermal runaway has occurred. The objective is to identify which cell/module arrangement is most critical within the battery pack, using microscopic analysis of the structure and chemical composition of the most damaged cells, both horizontally and vertically, of a battery belonging to a burnt vehicle. And their final condition was compared with the condition of new cells of the same type. In this way, the structure and chemical composition of the cathode, anode, and separator after thermal runaway were compared. This research was carried out to obtain information to understand the mechanical properties of lithium-ion cells and their behavior after thermal runaway heating leading to the propagation of a fire. Through the analysis carried out, it is concluded that cells placed in a vertical arrangement have worse behavior than cells in a horizontal arrangement. Regarding the safety of the battery, the results of this study will allow us to determine which arrangement and structure of the cells in the battery pack is safer against thermal runaway due to thermal failure.

Keywords: thermal runaway; pouch cell; chemical composition analysis; structural analysis; thermal failure test

1. Introduction

Battery fire safety remains an important concern due to high-temperature instability [1]. Over the past 30 years, there have been many accidents involving lithium-ion batteries, indicating that those batteries are not fire-safe. In addition, several serious fire accidents have occurred in Tesla Model S electric vehicles [2–7]. Some caught fire while being driven, and others during the charging and discharging process.

In general, lithium-ion batteries are most vulnerable when subjected to high temperature, electrical failure, or mechanical impact [8]. Lithium-ion batteries have limited temperature and voltage thresholds, and their components are unstable. Namely, the electrolyte is flammable, and the electrodes are made of a material with a high specific energy. All these characteristics imply this type of cell is prone to thermal runaway (TR) in some cases of abuse [9,10].

A lithium-ion battery may fail because of mechanical, electrical, or thermal failures that occur at the cell, module, or battery pack level (Figure 1). These failures occur in successive series, leading to the phenomenon of TR. Thermal failure due to overheating can occur, which may be due to incorrect contact connections or excessive heat near the battery pack, such as in a fire caused by combustion in a car accident. In addition, overheating may occur during fast charging as it uses high voltage and current levels. Thermal failure

can also be due to an internal short circuit, which occurs due to cell separator failures, manufacturing defects, or lithium build-up (dendrite formation) on the anode. This failure may also be due to defects originating during cell manufacture, which induce an internal short circuit.
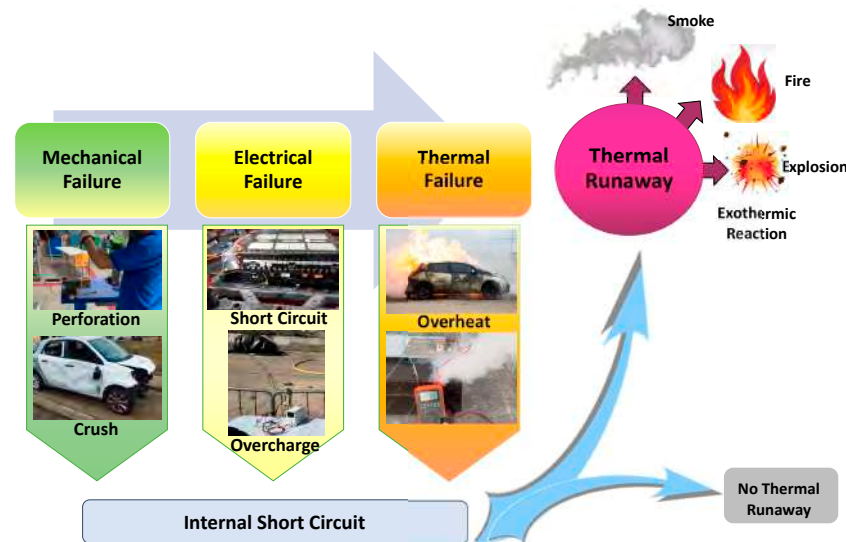

Figure 1. Failure mechanism related to lithium-ion battery failure and subsequent thermal runaway mechanism for electric vehicles (EVs) [11].

Thermal abuse failure due to external heat or flame exposure, which is also due to heat build-up inside from the incorrect removal of reaction heat or the initiation of unwanted internal exothermic reactions, can lead to thermal runaway. Controlled fire tests carried out on a complete electric vehicle with an installed high-voltage battery, such as scale tests with different cells and different cell arrangements, will allow characterization of the behavior of the cells in a fire due to electrical failure, high temperature, or significant deformation. The thermal runaway reaction is influenced by the stranded energy, which is the energy that remains stored inside the lithium-ion battery even after it has been discharged to a certain extent. In the context of a fire involving a lithium-ion battery, the stranded energy can represent a significant risk. To handle safely a lithium-ion battery involved in a fire, it is very important to be aware of the potential for trapped energy and to ensure that the battery is fully discharged and cooled before attempting to handle or transport it.

When a high-voltage battery is deformed or damaged, energy remains stored inside any undamaged battery cells and modules, and there is no way to discharge it. That stranded energy can cause a high-voltage battery fire in an electric vehicle to ignite several times after firefighters extinguish the fire. Emergency responders cannot measure how much energy remains inside a damaged battery, and they have no way of draining that energy. Engineers or other specialists can check the remaining voltage using the battery management system if the system is operational, and some high-voltage batteries have incorporated discharge ports. However, when an accident occurs, the high-voltage battery system can be damaged and deformed, making it impossible to access the battery management system or discharge ports. On the one hand, the duration of the post-crash fire and, on the other hand, the multiple reignitions of the battery could indicate that the battery contained stranded energy. Several researchers [12] from Oak Ridge National Laboratory conducted a study in which they concluded that lithium-ion cells with SoC > 80% subjected to mechanical damage were more prone to thermal runaway, while cells with a low SoC would not suffer thermal runaway but would only experience a slight temperature rise.

Several studies have been carried out to analyze the behavior of lithium-ion cells under external heating conditions. Huang et al. [13] heated three 50 Ah lithium-ion cells at different SoCs (States of Charge) with an electric heater and concluded that the cells

only turned on when the cell surface reached between 112 and 121 °C. The cell response and thermal runaway characteristics depend on the SoC. If the SoC is increased, then the time elapsed from heating to ignition is gradually reduced [13–15], and the reactions become more dangerous. Feng et al. [16] divided the internal chemical reactions occurring in lithium-ion batteries into different stages depending on the temperature reached. When lithium-ion batteries are overheated, their temperature gradually increases. The SEI (solid electrolyte interphase) film begins to break up when the cell reaches 90–130 °C [17]. As the SEI breaks up, the electrolyte reaches the graphite surface more easily and readily reacts with the intercalated lithium, releasing oxygen and generating more heat [18]. On the other hand, polyethylene (PE) can melt at 130–140 °C, causing an internal micro-short circuit and, thus, a continuous increase in battery temperature [19]. When the temperature reaches around 200 °C, the cathode materials start to decompose and release oxygen [20]. In addition, the decomposition reaction of the SEI film and the chemical reaction between the cathode metal oxide materials and the electrolyte is accelerated, as well as the reaction between the negative active substances and the electrolyte, which will produce more heat and gases [15] such as oxygen, HF, CO and NO [21–25]. As the temperature increases, the internal chemical reaction of the cell is much more complex and intense, generating a large amount of combustible gases and heat [26], followed by a thermal runaway reaction, causing subsequently the lithium-ion cell to burn or even at times explode.

It is important to understand the risk/hazard for the design of single cells and battery packs and modules to minimize or avoid the impact of thermal runaway. However, there are few studies on the methods of assessing the safety of cells or battery modules. Several studies have analyzed the influence of cell arrangement in a lithium-ion battery pack on thermal runaway (TR) propagation in both open and enclosed spaces [27]. Experimental results show that in a closed environment, when the battery's SoC is 100% and the cell spacing is more than 8 mm vertically and 4 mm horizontally, the possibility of thermal propagation for the battery pack is higher than that in an open environment. It is concluded that the TR propagation possibility of the battery pack in a vertical arrangement is higher than in a horizontal arrangement. Studies indicate that TR only occurs when the State of Charge (SoC) is higher than 50%. On the other hand, the critical spacing that triggers TR is 4 mm for a battery with an SoC at 80% and 6 mm for a battery with an SoC at 100% [28]. Feng et al. [29] conducted a mechanical failure (penetration) inducing TR on a module of six cells in series contact, concluded that the cell casing transfers the most heat, and developed a thermally resistant layer placed between the cells in order to prevent the propagation of TR in the module [30]. Lopez et al. [31] analyzed the influence of inter-cell spacing on TR and concluded that cell spacing in the battery pack is a critical factor as it greatly affects TR propagation. They analyzed different battery modules connected in series and concluded that the solution to TR propagation is good heat conduction. Therefore, there are several studies on the propagation of TR in series-connected battery modules [29–31], but there are few studies to analyze the propagation of TR in parallel-connected battery modules. Wike et al. [32] stated that the temperature increase after TR in a parallel-connected battery cell module is higher than if the cells in the module are connected in series. Lamb et al. [33] also found that the temperature increase in a module with parallel connected cells was higher, and as a result, the TR propagation was accelerated. Gao et al. [34] carried out a study of the propagation of TR in a large format battery module with parallel connections, 18 pouch cells in parallel 24 Ah. It is observed that the undamaged cells transfer the current to the cell experiencing TR, which causes it to experience a 10 °C higher temperature compared to a module with the cells connected in series. Therefore, a module with parallel connections is less safe.

In this study, overheating tests of a lithium-ion battery placed in an electric vehicle have been carried out using a fossil fuel heater to analyze how the arrangement of the cells influences the propagation of thermal runaway. The authors hope that this research can provide useful conclusions for the improvement of the Li-ion cell arrangement in electric

vehicles with the aim of reducing the damage caused by thermal runaway in lithium-ion batteries in automotive applications.

2. Materials and Methods

2.1. Methodology

The correctness of the results obtained will depend on the ability of the cell tests to reproduce the real behavior of a battery pack. As a starting point, a controlled fire test with a vehicle fitted with a battery pack was carried out to characterize its behavior.

2.1.1. Controlled Fire Test of an Electric Vehicle

Firstly, a controlled fire test was carried out on a complete electric vehicle, specifically a Nissan Leaf, in which the temperature progression and the behavior of the battery were analyzed. The fire was started by positioning a fuel burner on the bottom of the vehicle battery. Time and the battery temperature were monitored through the test with the help of a thermographic camera. The following Table 1 shows the main specifications of the battery analyzed.

Table 1. Specifications of the battery of the burnt Nissan Leaf vehicle.

Vehicle	Battery Electric Vehicle
Date of first registration	17 December 2015
Range	121 km (EPA test)
Battery specifications	
Capacity	24 kWh
Battery Voltage	360 V
Battery	Lithium-ion battery
Cell type	Laminate-type, pouch cells
Cathode Active Material	LMO ($LiMn_2O_4$) with NCA (lithium nickel-cobalt-aluminium oxide $Ni_{0.8}Co_{0.15}Al_{0.05}O_2$)
Anode Active Material	Graphite
Capacity	32.5 Ah
Nominal Voltage	3.75 V
Battery Modules	48
Cells per module	4
Energy Density	157 Wh/kg
Battery Weight	~180 kg
Battery Price	7000 €
State of Charge (SoC)	68.0%

The test started, and the vehicle was becoming hotter and hotter as the combustion process progressed. Within 3 min from the beginning of the test, the battery pack reached a temperature close to 805 °C. It was not until about eight minutes from the beginning that small explosions from the vehicle airbag gas generators began to be heard, followed by the phenomenon of thermal runaway in which the battery cells entered a self-heating and uncontrollable state.

Initially, the fire was extinguished using a fire blanket (Figure 2). After just over ten minutes from the beginning of the test, the temperature in the battery area exceeded 1000 °C. It was at this point that the firefighters proceeded to cover the vehicle with the blanket. Immediately after the vehicle had been covered by the blanket, the surface temperature of the vehicle dropped from approximately 850 °C to about 350 °C. From this moment on, the blanket insulates the vehicle from the radiation emitted by the fire, preventing any element from spreading into the environment and, at the same time, cooling the vehicle. In addition, the blanket prevents the oxygen supply, preventing the fire from continuing when all the oxygen confined under the blanket is consumed.

Figure 2. Zaragoza City Council firefighters covering the burnt vehicle with the fire blanket.

As the minutes passed, the temperature recorded by the thermal imaging camera dropped to around 100 °C. However, electric vehicle fires have a high risk of fire reignition because the battery continues to produce all the elements necessary for the fire to start—namely heat, fuel, and oxygen. If the vehicle is covered by the blanket, there is no risk, as it is only a matter of time before the battery temperature drops. But if the vehicle is uncovered, the risk of a restart is very high. This is why 9 min after, the vehicle was completely covered, it was decided to remove the blanket to show how the process of restarting the fire is reproduced. Just after removing the blanket, it can be seen how the fire restarts from the battery area and quickly spreads again throughout the vehicle.

As the test continued, the fire increased again the temperature during the following two and a half minutes, reaching a peak temperature of around 600 °C. Once this temperature is reached, the vehicle is covered again to insulate and extinguish the vehicle fire again, given that the blanket is reusable.

The following shows the state of the battery pack (Figure 3a) and a detailed view of the battery modules (Figure 3b) before the fire test:
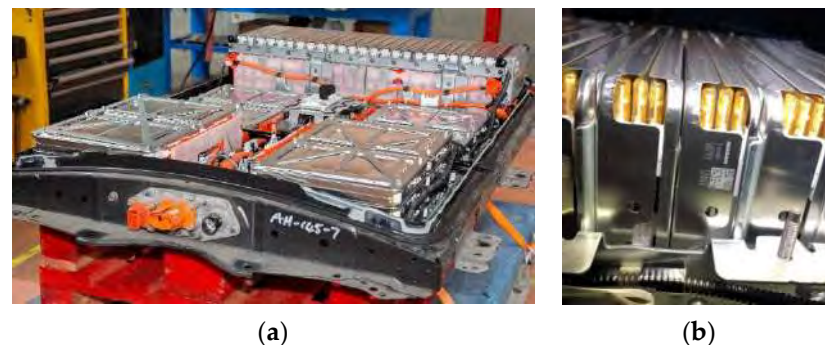

(**a**)   (**b**)

Figure 3. (**a**) Battery pack before fire test. (**b**) Detail of a battery module constructed with a 4-cell configuration).

To finalize the test, once the blanket was removed, the battery was cooled with water and the vehicle was left in quarantine to check that the fire did not restart.

The following table (Table 2) gives details of the fire test specifications:

Table 2. Characteristics of the controlled fire test carried out on the Nissan Leaf vehicle.

Fire test specifications	
Place and date	Zaragoza, 5 December 2019
Vehicle under test	Battery Electric Vehicle
TEST	
Vehicle	Vehicle only with voltage battery
Fire	Ignition Burners (fossil fuel)
Method to extinguish the fire	Bridgehill Car Fire Blanket
Temperature monitoring	Thermal Imaging Infrared Camera: FLIR T640
Thermal Imaging Infrared camera distance	13.7 m
Ambient Temperature	7.1 °C
Average Wind Speed	2.5 m/s
Maximum Wind Speed	8.9 m/s
Maximum Temperature reached	~1000 °C
Time to start Battery Thermal Runaway	~8 min
After removing the blanket	
Amount of water to extinguish the fire	400 L

Images of the electric vehicle fire test explained above are shown below (Figure 4):
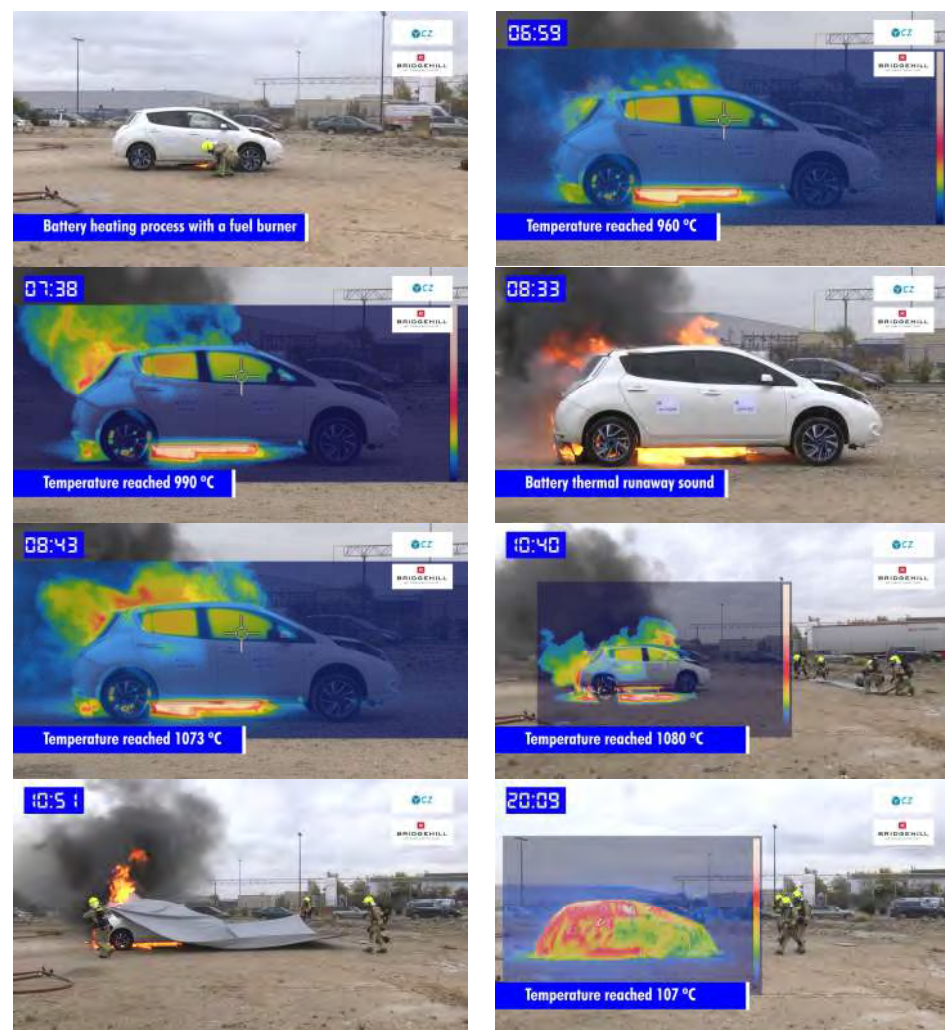

Figure 4. Images of the controlled fire test carried out on the Nissan Leaf vehicle under study.

Figure 4 shows a series of images of the fire test carried out. On left upper corner, the time elapsed in minutes since start of the vehicle ignition is shown. Within 7 min from

the start of the test (second image upper right), the battery pack reached a temperature close to 960 °C. It was not until about eight minutes from the begging that small explosions from the vehicle airbag gas generators began to be heard, followed by the phenomenon of thermal runaway in the battery cells (fourth image). The range of the thermal event onset temperature is 80–150 °C.

2.1.2. Identification of the Most Damaged Cells in the Analyzed Battery

Once the test had been carried out and the necessary quarantine time had elapsed, the cells were dismantled (Figure 5) to see how they behaved and their condition according to the position they were in. The aim was to analyze how the enclosure was damaged according to the position of each cell within the enclosure. Moreover, deformation suffered by each of the cells was studied. Finally, the condition of these cells has been perfectly documented.
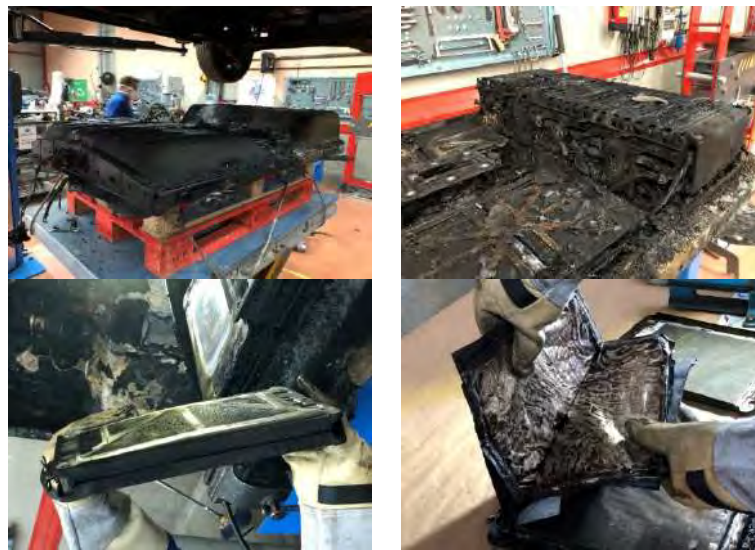

Figure 5. Pictures of the state of the battery pack, the module, and the lithium-ion cells inside the battery pack.

Once the burnt battery of the Nissan Leaf had been disassembled, the most damaged modules were visually identified, being those modules that showed the greatest deformation and breakage, both vertically (module 11) and horizontally (module 30), and all modules were disassembled and visually analyzed.

In Figure 6 a number has been assigned to each of the battery modules in order to identify them.
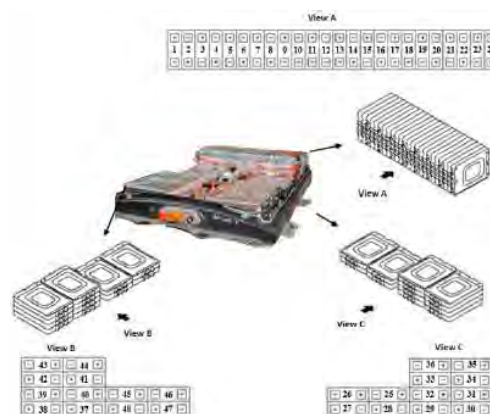

Figure 6. Exploded view and module identification of the traction battery of a first-generation Nissan Leaf.

Figure 7 shows burnt Nissan Leaf battery disassembled in the arrangement in which it is in the vehicle.

Figure 7. Burnt Nissan Leaf battery disassembled in the arrangement in which it is in the vehicle.

The following pictures show the state of the most damaged modules, firstly, Figure 8 shows the state of the burnt Nissan Leaf vehicle battery module 30 and secondly, Figure 9 shows the state of the burnt Nissan Leaf vehicle battery module 11:

Figure 8. Images of the condition of module 30 (horizontal arrangement) of the battery pack of the burnt Nissan Leaf vehicle. This module has been identified as the most damaged among the modules in the horizontal arrangement.
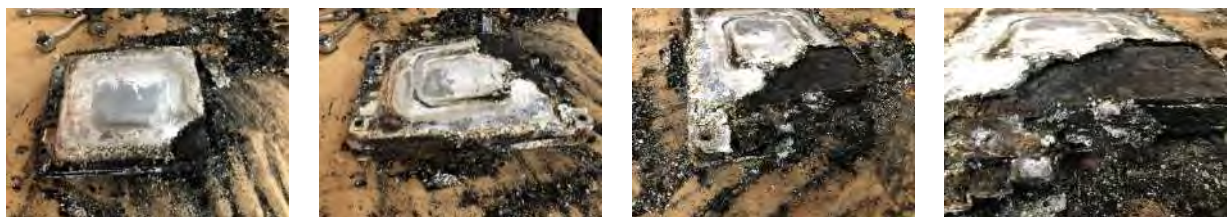

Figure 9. Images of the condition of module 11 (vertical arrangement) of the battery pack of the burnt Nissan Leaf vehicle. This module has been identified as the most damaged among the vertically arranged modules.

The following Figure 10 identifies the position of the most damaged modules in the battery pack analyzed:
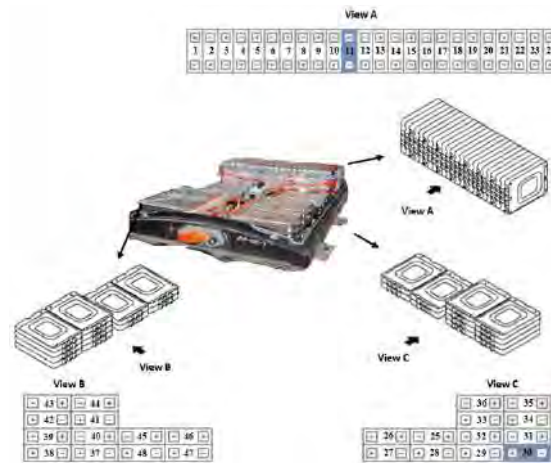
Figure 10. Exploded view of the first-generation Nissan Leaf battery, with identification of the most damaged modules, shaded in blue.

2.1.3. Generation of Samples for Structural and Cross-Sectional Analysis

A study of the structure was carried out by taking samples and analyzing them transversally (there are several layers of anodes and cathodes, as well as separators; it is a stack sample of materials) (see Figure 11), and on the other hand, a surface analysis of the chemical composition was carried out. To perform that, anode, cathode, and separator were separated (see Figure 12).

For the structure analysis test, three transversal section samples were taken from a cell of module 11, three transversal section samples from a cell of module 30, and two transversal section samples from a new cell. For chemical composition and morphology analysis, one sample was taken from the cathode, one sample from the anode, and one sample from the separator for module 11, module 30, and the new cell, respectively. The samples for the tests were obtained at Centro Zaragoza facilities, and once the samples had been obtained, the tests were carried out at the Material Science Department of the University of Zaragoza. Sampling has been carried out considering the indications of a previous study [35]. Images from sample preparation to Sibe tested for the new cell are shown below.
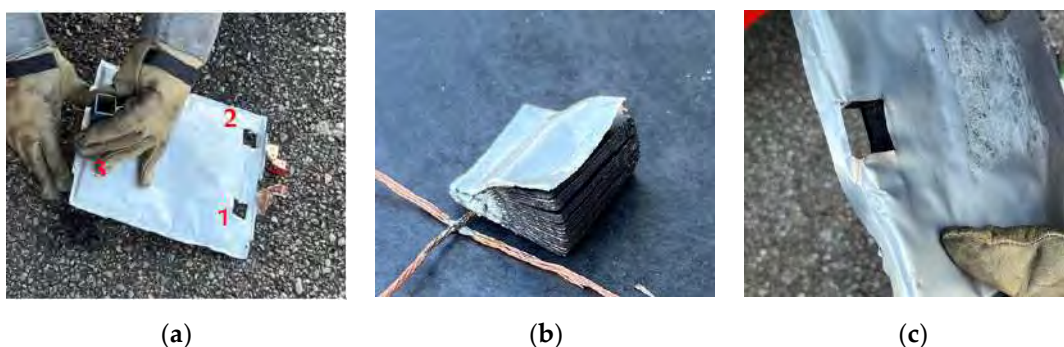

(**a**) (**b**) (**c**)

Figure 11. Sample and obtaining the sample for structural analysis. (**a**) Location of the points from where the samples have been obtained for the structural analysis of the stacked layers: 1. Anode tab (copper); 2. Cathode tab (aluminum); 3. (**b**) Sample generated in position 3. (**c**) Section of the pouch cell once the sample has been extracted.
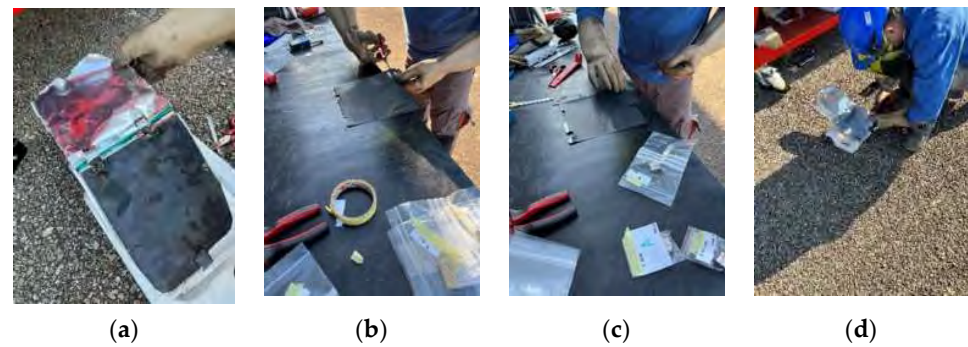
Figure 12. Obtaining the sample for surface analysis. (**a**) Image of the inside of a pouch cell from where the samples for surface analysis of the stacked layers (anode, cathode, and separator in the case of the intact cell) have been obtained. (**b**) Sample generated from the anode (copper tab). (**c**) Sample generated from the cathode (aluminum tab). (**d**) Sample generated from the separator.

Figure 13 below shows the position from which samples have been taken from a calcined cell of module 30:

Figure 13. Obtaining samples from a module 30 calcined cell. The letters A–D identify the cell within the module and the numbers 1–3 indicate the position from which the sample has been taken.

For the preparation of the surface sections of the individual layers, after obtaining the samples, with a surface area of approximately 5 mm × 5 mm, of each of the different layers of the cell, anode, cathode, and separator (in the case of the new cell), they were coated with a layer of high purity carbon of 10.40-nanometer thick carbon layer to make them conductive, using a Leica EM ACE600 sputtering coater, (Leica Microsystems, Spain) and placed on an aluminum support with a double-sided carbon adhesive tape so that they do not move from the support during the analysis. A small sample of cobalt is placed to calibrate the equipment.

After obtaining the samples, with a surface area of approximately 10 mm × 10 mm, from the electrode stack, the samples are embedded in resin to improve the preparation result and then polished so that the surface is scratch- and deformation-free, flat, and highly reflective. A prepared sample embedded in resin is shown below (Figure 14).
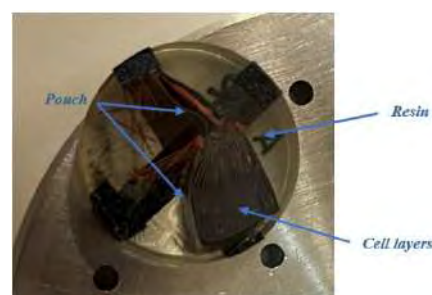

Figure 14. Layer structure of a resin-embedded and polished cell, used to identify cell parameters and cell structure.

2.1.4. Method for Carrying Out the Surface and Structural Analysis

A Carl Zeiss MERLINTM (Carl Zeiss SMT AG, Germany) Field Emission Scanning Electron Microscope (FESEM) was used to perform the analyses. It has a hot-field emission electron emission cannon and allows observations up to 0.8 nm spatial resolution and acceleration voltages between 0.02 and 30 kV. It has secondary and backscattered electron detectors in the chamber and in the column (in-lens). It also has an EDS detector for analysis of the energy of X-Max scattered X-rays (20 mm^2) with SDD (Silicon Drift Detector) from Oxford Instruments (United Kingdom). For the generation of images in scanning electron microscopy, the interaction products most frequently used are secondary electrons (SEs) and backscattered electrons (BSEs). For the distinction and detection of SEs and BSEs, it must consider two parameters: energy and angle distribution. For that mission, an energy-selective backscattered detector (EsB) and an angle-selective backscattered detector (AsB®) have been used. The standard detectors are the in-lens detector (annular SE detector), which detects SE signals and is used to analyze surface structure, and the SE2 detector (Everhart-Thornley type), which detects SE2 signals and is used to analyze topography.

Morphology can be analyzed with SE2 and in lens, backscattered and low-energy backscattered EsB (different gray level due to different chemical composition), and high-energy backscattered AsB.

The following Table 3 show information on different detectors used by the FESEM:

Table 3. Information on the different detectors used by the FSEM.

Standard Detectors	Detected Signals	Typical Application
In-lens detector (annular SE detector)	SE	Surface Structure
SE detector (Everhart-Thornley type)	SE2	Topography
Optional Detectors	**Detected Signals**	**Typical Application**
EsB® detector with filtering grid (in-column detector)	BSE	Pure material contrast
AsB® detector, integrated	BSE	Channeling contrast (cristal orientation), compositional contrast

The SE2 detector detects SEs as well as BSEs. Electrons on the way to the detector are grouped by the collector and directed to the scintillator. The collector voltage (suction voltage), with a range between −250 V and +400 V, generates an electrical field located in front of the detector, thus directing the low-energy SEs toward the scintillator. The collector bias should be set to +300 V for all standard applications. The whole AsB® angular selective backscattered electron detector is built within the GEMINI® lens's pole piece. This eliminates the need to align the AsB® detector with the optical axis in order to image BSEs at extremely small working distances. It is possible to distinguish between low-angle and high-angle BSEs with this detector arrangement. The AsB® detector is equipped with four diodes, and each can be individually adjusted via a menu. While the topography mode displays surface features, the compositional mode generates images that display the specimen's atomic contrast. Secondary electrons have an energy <50 eV and are inelastically scattered primary electrons. They are produced from the adjacent surface of the incoming primary electron beam, providing the best lateral resolution when it comes to several nanometres. The backscattered electrons disperse elastically in the field of the atomic nucleus. The energy range is from >50 eV to the excitation energy. When the atomic number or atomic weight of a phase or region is higher, a greater number of electrons will be backscattered from this area of the sample (material contrast).

The Figure 15 below shows two views of the surface tests carried out.

Figure 15. Views of the surface tests carried out.

2.1.5. Method for Carrying Out the Chemical Analysis

To obtain information on the chemical composition of the analyzed surface, electron energy loss spectroscopy combined with electron microscopy was used. To do this, high-energy electrons were directed toward the samples, which caused the electrons in the inner shell to ionize, creating a vacancy in the inner layer. This unfilled position is occupied by an electron of a higher energy level, releasing energy that might be observed as an X-ray quantum or Auger electron (electron that is forced to leave the atom). This energy, known as X-ray radiation, is unique to each element. An EDAX Super Octane (EDAX, Pleasanton, CA, USA) silicon drift detection system (energy resolution of about 123 eV @ Mn Ka) with a silicon nitride window for optimal sensitivity in the low-energy region was used to capture the EDX spectra.

3. Results and Discussion

The conclusions obtained from the microscopic analysis of lithium-ion cells are the basis for research into the operation, safety, and degradation of lithium-ion batteries. There are studies [35] in which analyses have been carried out using images taken under a microscope to obtain information that allows us to understand the mechanical properties of lithium-ion cells. Parameters such as layer thickness, material composition, and surface properties are important in the analysis and further development of lithium-ion batteries. The purpose of this section is to compare the structure and chemical composition of the anode, cathode, and separator in cells that have undergone thermal runaway compared to an intact (new) cell.

In this section, not only the methods used to procure the surface properties and chemical composition of all the batteries but also the results of SEM images of transverse sections of zone 1 (Anode) of an original cell and a cell from module 11 and module 30 of the burnt Nissan Leaf vehicle battery are presented. The surface properties and chemical composition of the different components of an original cell and a burnt cell from module 11 and module 30 are also analyzed.

3.1. Surface Test Results: Surface Properties and Chemical Composition Analysis

To carry out the surface analysis tests, three aluminum supports are prepared: support A, support B, and support C. Two cathode samples, one from the upper cathode and one from the lower cathode, and two anode samples, one from the upper anode and one from the lower anode, are prepared in support A from cell B of module 30. Two cathode samples, one from the upper cathode and one from the lower cathode, and two anode samples, one from the upper anode and one from the lower anode, are prepared in support B from cell C of module 11. And in support C, a sample of the cathode, anode, and separator of a new Nissan Leaf cell is prepared.

The following images (Figure 16) compare different pictures obtained with FESEM of the upper cathode of module 30, module 11, and the new cell.
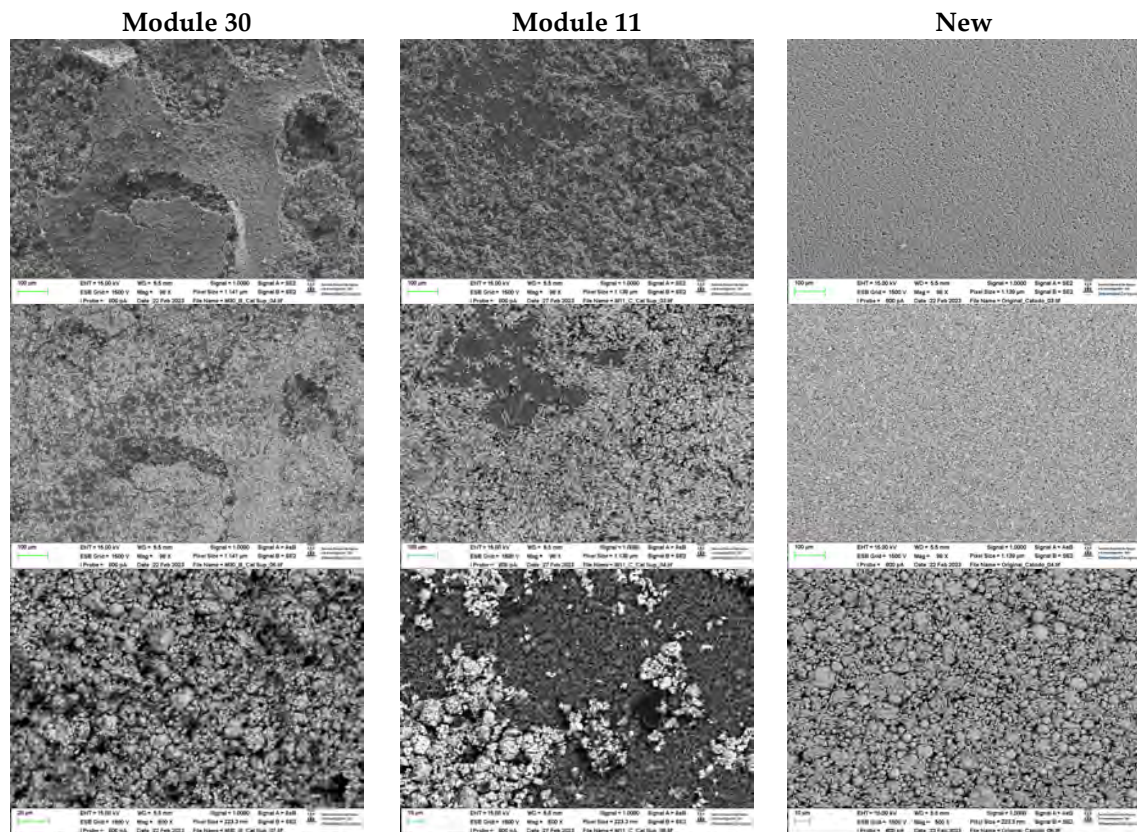
Module 30	Module 11	New

Figure 16. Comparison of images obtained with the FESEM of different areas of the upper cathode of module 30, module 11, and the new cell.

The following images compare different images obtained with FESEM of the lower cathode of module 30, module 11, and the new cell.

With respect to the cathode electrodes in the figure above, the cathode of an original cell has been compared with two cathodes (one upper and one lower) of module 30 and module 11 of the battery of the burning Nissan Leaf after experiencing the thermal runaway. It should be remarked that rather than a single particle size, most materials, especially the active materials used in battery electrodes, contain a variety of particle sizes.

It is noted in Figure 17 that after experiencing the thermal runaway phenomenon, the cathode surface is covered with off-white floccules. The distribution of these floccules on the surface of the cathode electrodes is not uniform, being more concentrated in one area and more dispersed in another area.

Due to the morphology of these substances, it can be deduced that they are decomposed separators due to the high temperature since, at 150 °C, the separator shrinks and groups together. In other words, after TR, the separator decomposes as the temperature increases.

The temperature of decomposition of a PE-PP-based polymer is more than 300 °C. Therefore, it is appropriate to cover the surfaces of the cathode electrodes with unevenly distributed separator particles.
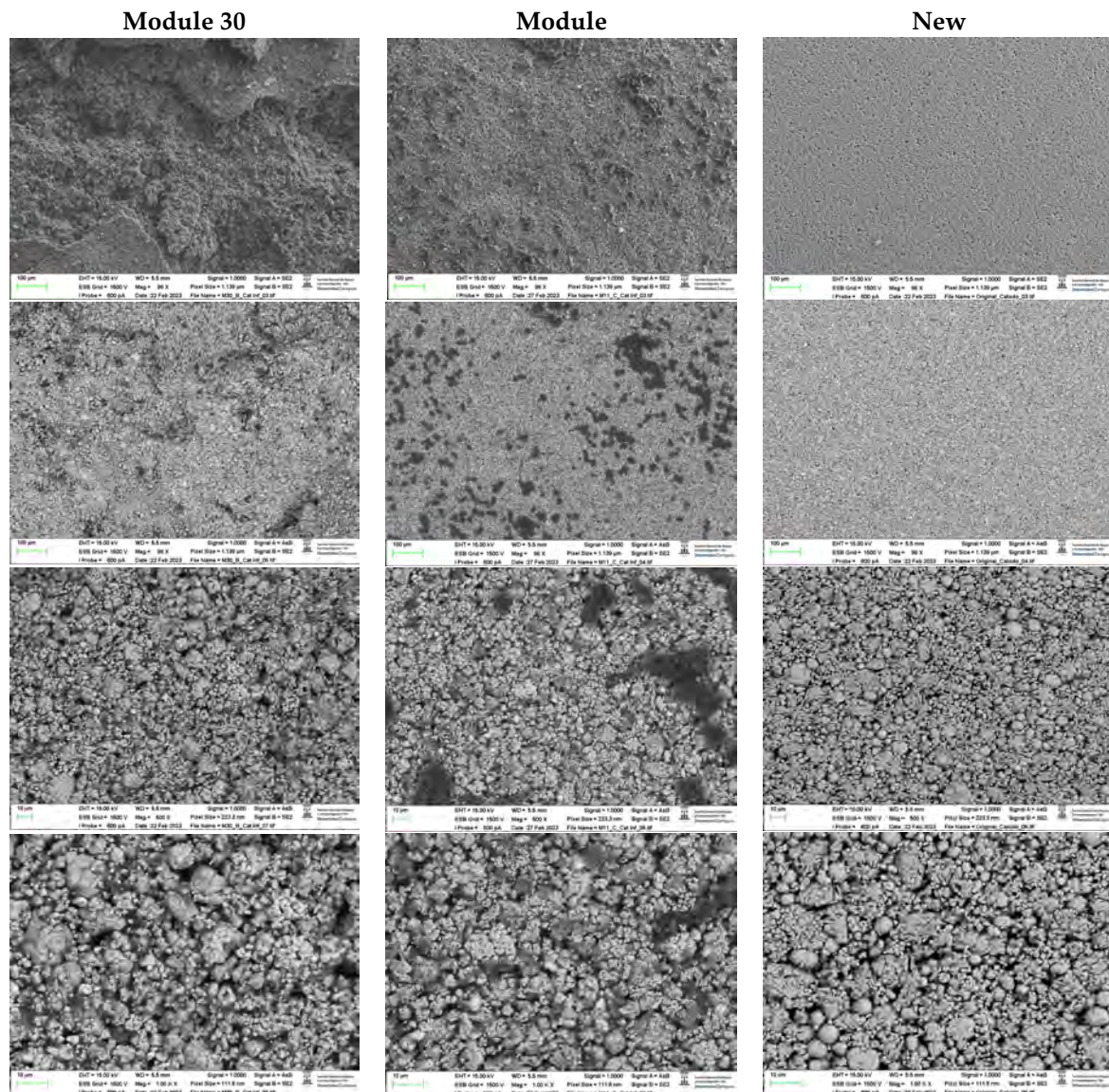
Module 30   Module   New

Figure 17. Comparison of images obtained with the FESEM of different areas of the lower cathode of module 30, module 11, and the new cell.

It should be noted that the burned modules being analyzed had a 68% SoC (State of Charge). As the SoC increases, the number of flocs increases greatly, and darker-colored and spherical flocs appear, indicating that having an elevated SoC during TR, the reaction temperature inside the cell is higher, and the agglomeration and decomposition reactions of the separators are more intense [36].

After TR, the spherical cluster structure of the cathode active materials and the flake structure of the graphite were destroyed. The cathode and anode are joined together, and it is difficult to identify them (Figures 5 and 13). There are also irregularly shaped impurities/debris, some rectangular and some spherical, and they are chaotically distributed. When the temperature is increased due to the TR, the aluminum current collector of the chaotic electrode had oxidized and adhered to the anode side.

Therefore, it is normal to observe in the cathode traces of fragments of cathode materials after TR, ash from the separators and cathode material, and products of exothermic reactions and graphite peels (Figure 17, images of the last row).

It is observed that in the case of module 11, there are more dark-colored flocs than in the case of module 30, and there are more in the upper cathode than in the lower cathode. Therefore, it is concluded that module 11, in a vertical arrangement, experiences a higher

temperature in the TR at the same SoC as module 30, which is in a horizontal arrangement. If the structural transformation (morphology analysis with InLens) of the cathode materials after the TR is analyzed (Figures 18 and 19), it is observed that in the case of modules 30 and 11 with a SoC of 68% after the TR, the layered structure of the material was destroyed, the resulting particles dispersed out of the original layered structure and subsequent adhesion occurred. The cathode (positive electrode) material reacted at high temperatures and decomposed. On the other hand, carbon particles from the anode (negative electrode) were doped into the cathode (positive electrode) through the damaged diaphragm.

Module 30	Module 11	New

Figure 18. Morphological analysis of the transformation of the upper cathode of Module 30 and Module 11 after the thermal runaway compared with the initial cathode structure of a new cell.

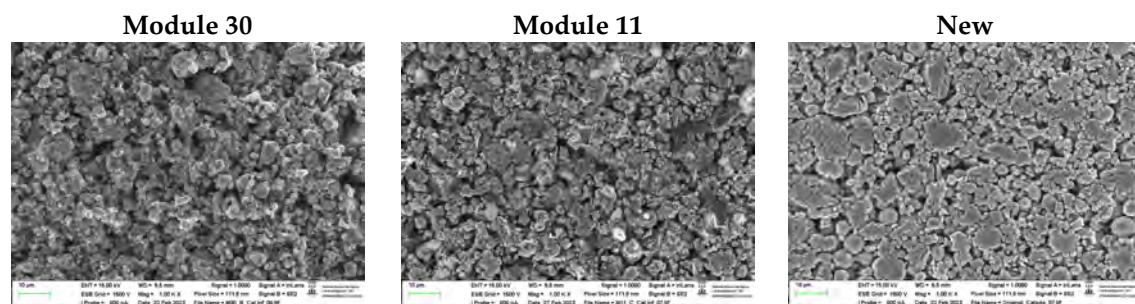| Module 30	Module 11	New

Figure 19. Morphological analysis of the transformation of the lower cathode of Module 30 and Module 11 after the thermal runaway compared with the initial cathode structure of a new cell.

It is observed that in the case of the lower cathode of module 30 (horizontal arrangement), the particles are smaller compared to the upper cathode of module 30; this may be due to the higher temperature as it is more exposed.

In the case of module 11 (vertical arrangement), there is no difference between the particle size of the upper cathode and the lower cathode. Hereafter, the chemical composition analysis of the upper cathode of module 30 and module 11 will be presented in comparison to the composition of the original cathode. The cathode showed a granular surface structure, as can be seen in the following image (Figure 20). The largest particles were about 6 μm in size. The following chemical elements were identified by EDXS: nickel (Ni), manganese (Mn), cobalt (Co), oxygen (O), and carbon (C). This led to the conclusion that this compound has the chemistry of a $LiNiMnCoO_2$ (NMC) cathode. Two different types of compounds were observed on the cathode surface, marked in Figure 21 by two red boxes. The results of a detailed analysis of the formed compounds show that the compound marked with "1" had the NMC chemistry mentioned above, while the second compound was determined to be a manganese oxide compound (LMO), some fluorine was also observed that may be from the electrolyte (LiPF6) when in contact with the cathode and anode. Considering these issues, cathode layer chemistry could be concluded as a mixture of NMC and LMO.
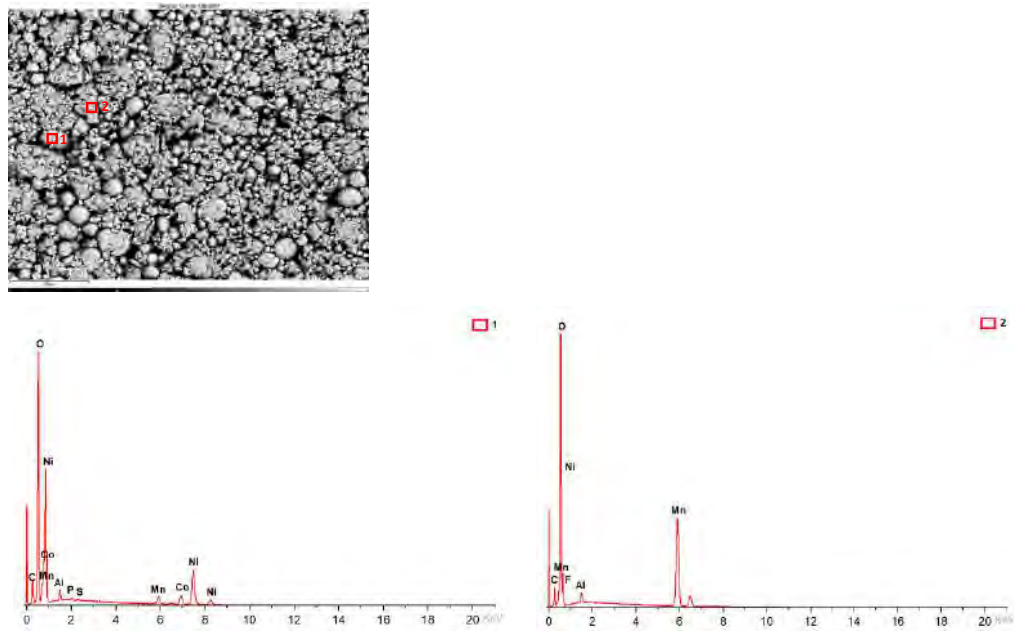
Figure 20. Chemical composition of the original cathode.

During the EDXS measurement, different areas were focused on, and the corresponding peaks are shown in Figure 20. Details of the two spectra of the component values measured in atomic and weight % are listed in Table 4.

Table 4. EDXS weight ratio of components in original cathode using two spectra focused on two distinct areas.

		C		O		F		Al		Mn		Co		Ni	
		Weight (%)	Atomic (%)	Weight (%)	Atomic (%)	Weight (%)	Atomic (%)	Weight (%)	Atomic (%)	Weight (%)	Atomic (%)	Weight (%)	Atomic (%)	Weight (%)	Atomic (%)
Compound 1: LiNiMnCoO$_2$	Spectrum 1	8.46	19.32	29.5	50.6			1.42	1.44	3.89	1.94	9.57	4.45	46.69	21.82
Compound 2; LMO + F	Spectrum 2	5.19	11.84	31.29	53.52	2.54	3.66	1.17	1.19	59.8	29.79				

Next, the chemical composition of the upper cathode of the ignited module 30 is analyzed. The upper cathode of module 30 no longer shows a defined granular surface, as in the case of the original cathode; the structure was broken. The largest particles are about 5 μm in size. The following chemical elements were identified by EDXS: nickel (Ni), manganese (Mn), cobalt (Co), oxygen (O), fluorine (F), phosphorus (P), carbon (C), and aluminum (Al). Two different compound types were observed on the cathode surface of module 30, marked in Figure 21 by two red crosses. The results obtained from an exhaustive analysis of the formed compounds show that the compound marked with "1" had the chemistry of a compound with manganese and oxygen and some fluorine and phosphorus, while in the rectangular-shaped compound "3" fluorine and nickel were observed. This last compound is due to the reactions that have taken place in the TR, and that is why there are leftovers of the electrolyte.
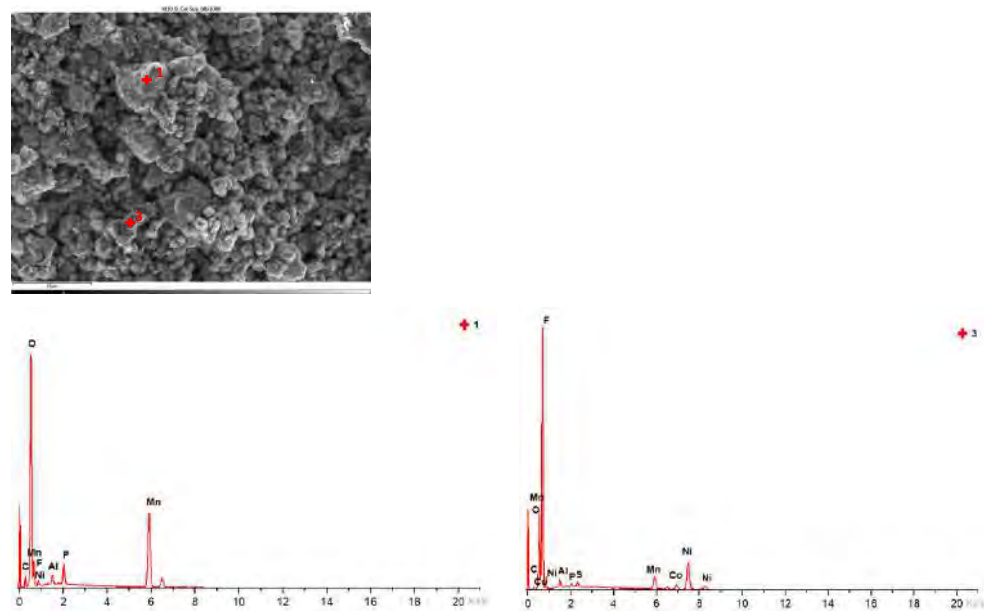
Figure 21. Chemical composition of the upper cathode of module 30.

During the EDXS measurement, different areas were focused on, and the corresponding peaks are shown in Figure 21. Details of the two spectra of the component values measured in atomic and weight % are listed in Table 5.

Table 5. EDXS weight ratio of components in the upper cathode of the ignited module 30 using two spectra focused on two distinct areas.

		O		F		Al		P		Mn		Ni	
		Weight (%)	Atomic (%)	Weight (%)	Atomic (%)	Weight (%)	Atomic (%)	Weight (%)	Atomic (%)	Weight (%)	Atomic (%)	Weight (%)	Atomic (%)
Compound 1: Mn and O, with some F and P	Spectrum 1	26.91	50.88	6.7	10.66	1.26	1.41	2.94	2.87	60.38	33.24	1.81	0.93
Compound 2: F and Ni	Spectrum 2	30.55	47.88	20.86	27.54	4.49	4.17	1.47	1.19	34.57	15.78	7.19	3.07

Next, the chemical composition of the lower cathode of the ignited module 30 is analyzed. The lower cathode of module 30 also does not show a defined granular surface, as in the case of the original cathode; the structure was broken. The larger particles are about 4 μm in size, so the particles are smaller than in the case of the upper cathode of the same module, probably because they have been exposed to higher temperature values. Two different compound types were observed on the surface of the lower cathode of module 30, marked in Figure 22 with two red crosses. A detailed analysis of the compounds obtained shows that the compound marked with "1" had the chemistry of a compound with oxygen and manganese, while it was determined that the second structure was also the chemistry of a nickel and oxygen compound; some manganese, fluorine, cobalt, and aluminum were also observed.

During the EDXS measurement, different areas were focused on, and the corresponding peaks are shown in Figure 22. Details of the two spectra of the component values measured in atomic and weight % are listed in Table 6.

The distribution of elements in each area of the upper cathode of module 30 is also mapped. This information is also collected with the EDS detector and then processed with the AZtec software (Figure 23).
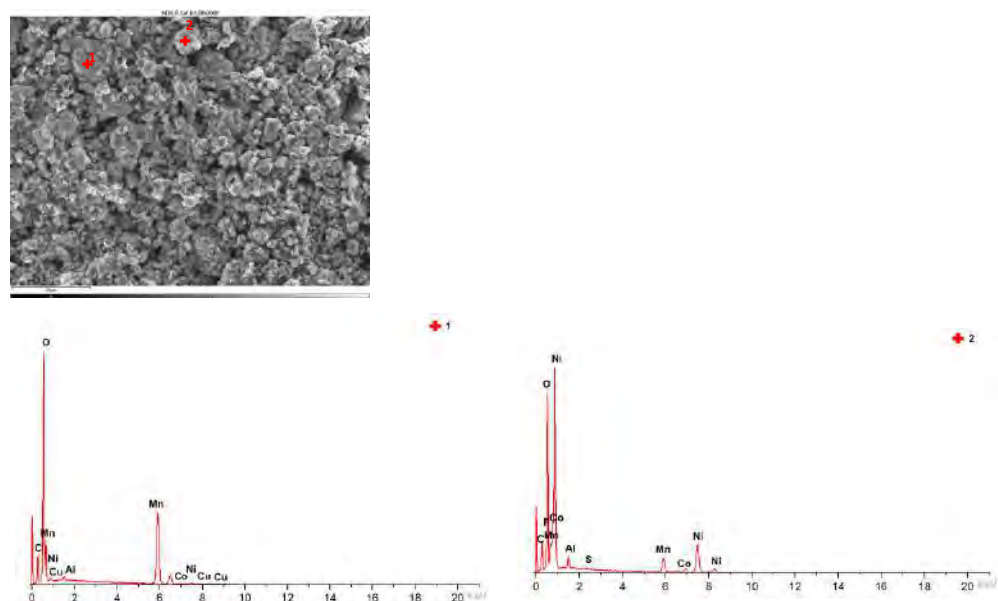
Figure 22. Chemical composition of the lower cathode of module 30.

Table 6. EDXS weight ratio of components in the lower cathode of the ignited module 30 using two spectra focused on two distinct areas.

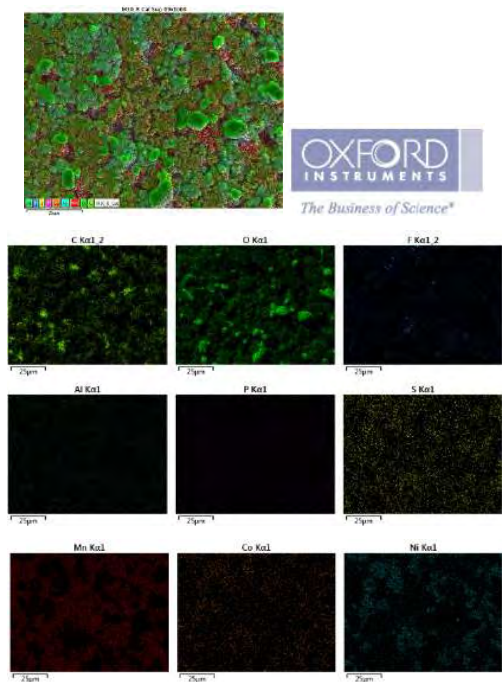|		O		F		Al		Mn		Co		Ni	
		Weight (%)	Atomic (%)	Weight (%)	Atomic (%)	Weight (%)	Atomic (%)	Weight (%)	Atomic (%)	Weight (%)	Atomic (%)	Weight (%)	Atomic (%)
Compound 1: O and Mn	Spectrum 1	29.71	59.05			0.59	0.7	67.4	39.01	0.74	0.4	1.56	0.85
Compound 2: O and Ni, with some Mn, F, Co and Al	Spectrum 2	24.77	49.88	6.17	10.46	2.04	2.43	10.63	1.19	5.68	3.1	50.56	27.74

Figure 23. Distribution of elements in each area of the upper cathode of module 30.

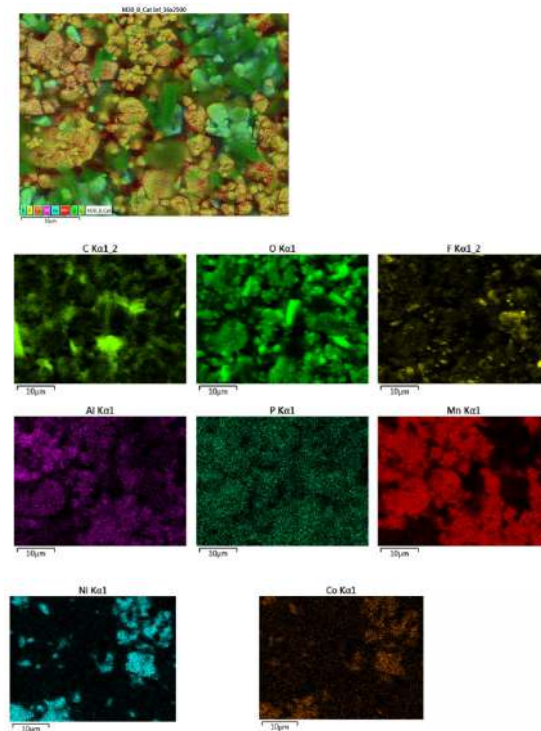Below (Figure 24) is a map of the distribution of elements in each area of the lower cathode of module 30.

Figure 24. Distribution of elements in each area of the lower cathode of module 30.

In the lower cathode, there is a higher amount of fluorine, aluminum, manganese, phosphorus, nickel, and cobalt than in the upper cathode. The following figure shows the chemical composition of the upper cathode of modulo 11. The upper cathode of module 11 also does not show a defined granular surface, as in the case of the original cathode; the structure was broken. The larger particles are about 5 μm in size, so the particles are smaller than in the case of the original cathode. Three different types of structures are observed on the surface of the upper cathode of modulo 11, marked in Figure 25 with three red squares.
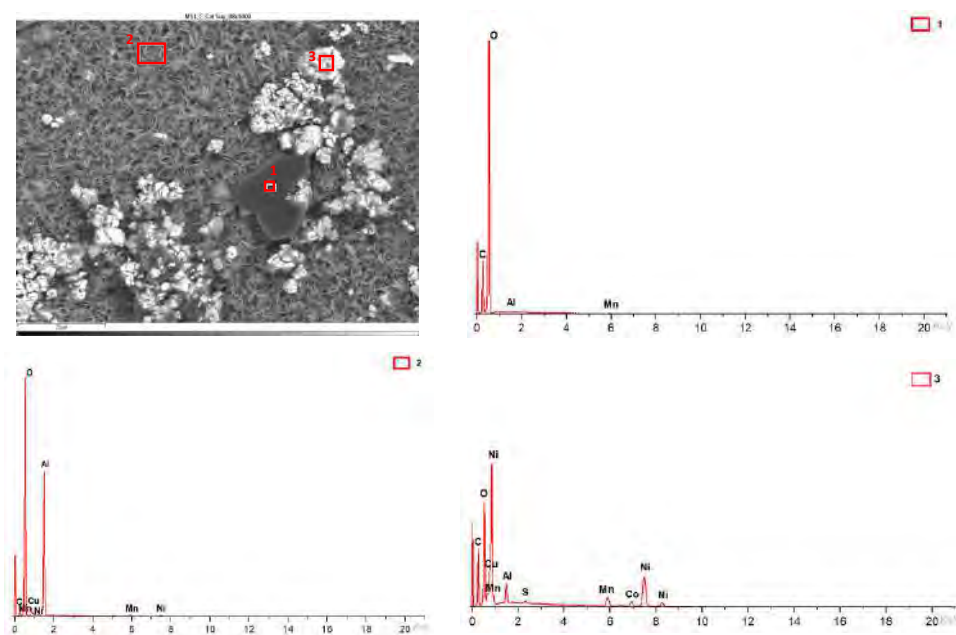

Figure 25. Chemical composition of the upper cathode of module 11.

Details of the three spectra of the component values measured in atomic and weight % in the upper cathode of module 11 (Figure 25) are listed in Table 7.

Table 7. EDXS weight ratio of components in the upper cathode of the ignited module 11 using three spectra focused on three distinct areas.

		C		O		Al		Mn		Co		Ni	
		Weight (%)	Atomic (%)	Weight (%)	Atomic (%)	Weight (%)	Atomic (%)	Weight (%)	Atomic (%)	Weight (%)	Atomic (%)	Weight (%)	Atomic (%)
Compound 1: C and O	Spectrum 1	17.92	22.61	81.51	77.2	0.12	0.07	0.44	0.12				
Compound 2: O and Al	Spectrum 2	6.49	9.97	60.91	70.18	25.88	17.68	2.79	0.94			3.93	1.23
Compound 3: C, O and Ni, with some Al, Mn and Co	Spectrum 3	23.4	47.63	17.05	26.05	2.59	2.35	5.46	2.43	5.51	2.29	45.69	19.03

A thorough analysis of the chemicals that were created reveals that the compound marked with "1" had the chemistry of a carbon and oxygen compound, while the second structure was determined to be an aluminum and oxygen compound, formed from the fusion of the cathode aluminum collector, and the third structure was a chemical compound containing nickel, carbon, oxygen, cobalt, manganese, and aluminum. They are all elements that are products of the cathode and collector coating. Regarding module 11, a higher amount of aluminum is observed; this may be since, in this case, the aluminum collector has been more damaged than in the case of module 30.

The following Figure 26, shows the chemical composition of the lower cathode of module 11. The lower cathode of module 11 also does not show a defined granular surface, as in the case of the original cathode; the structure was broken. Five different types of compounds are observed on the surface of the lower cathode of module 11, shown in Figure 26. A detailed analysis of the compounds formed reveals that the compound marked with "1" had peaks of nickel, manganese, oxygen, copper, carbon, cobalt, and fluorine, so it presents all the elements of the cathode coating; there is also copper that can come from the anode collector. The second structure was a compound of nickel, manganese, cobalt, oxygen, and carbon, and the third structure was a compound of copper and oxygen, probably because the anode collector had melted. If compound 4 is analyzed, it is a nickel, oxygen, manganese, and fluoride-containing chemical compound. And finally, compound 5 is a manganese and oxygen compound formed from the active material of the cathode, and there is also aluminum coming from the aluminum collector of the cathode. In this area, an aluminum peak appears; this is the result of a thermal failure that leaves the aluminum current collector exposed.

During the EDXS measurement, different areas were focused on, and the corresponding peaks are shown in Figure 26. Details of the five spectra of the component values measured in atomic and weight % are listed in Table 8.
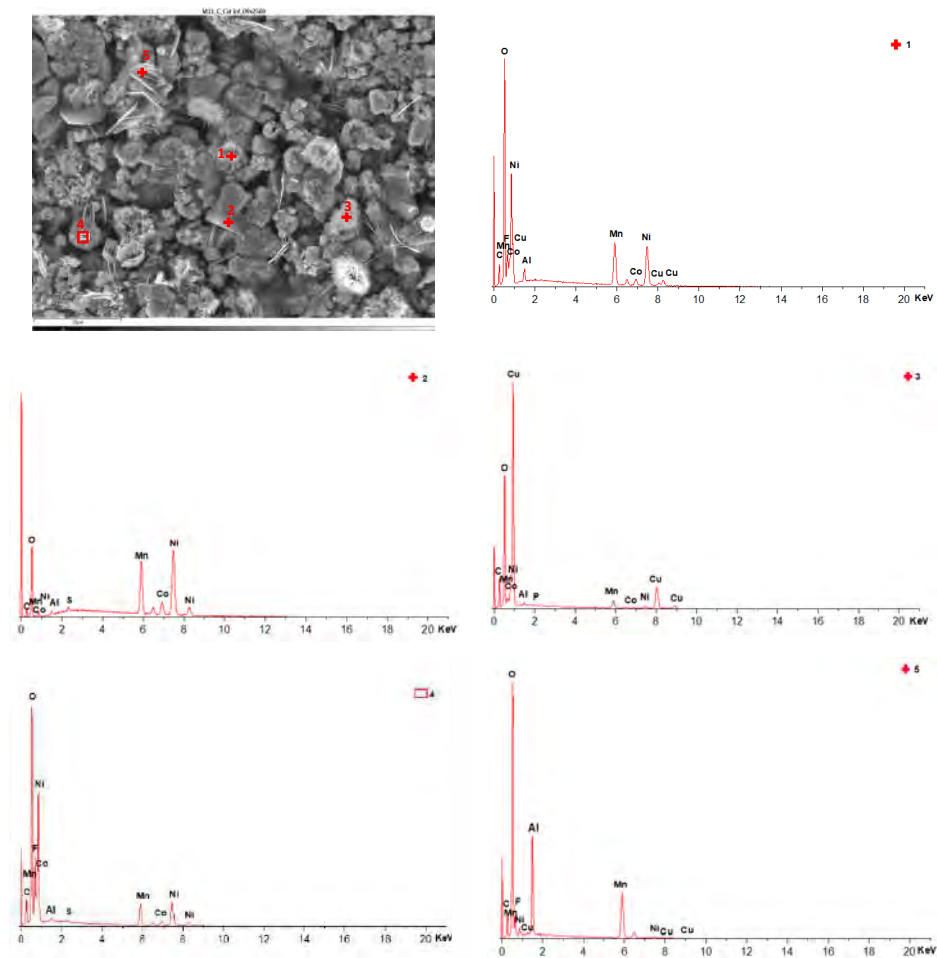
Figure 26. Chemical composition of the lower cathode of module 11.

Table 8. EDXS weight ratio of components in the lower cathode of the ignited module 11 using five spectra focused on five distinct areas.

	C		O		F		Al		Mn		Co		Ni		Cu	
	Weight (%)	Atomic (%)	Weight (%)	Atomic (%)	Weight (%)	Atomic (%)	Weight (%)	Atomic (%)	Weight (%)	Atomic (%)	Weight (%)	Atomic (%)	Weight (%)	Atomic (%)	Weight (%)	Atomic (%)
Spectrum 1 Compound 1: Ni, Mn, O, Cu, C, Co with F	5.73	15.49	17.97	36.46	4.28	7.32	1.08	1.3	18.06	10.67	4.4	2.42	37.3	20.62	11.19	5.72
Spectrum 2 Compound 2: Ni, Mn, Co, O, C	2.02	7.83	5.95	17.34			0.36	0.61	21.87	18.56	9.06	7.17	60.4	47.98		
Spectrum 3 Compound 3: Cu and O	14.26	33.54	20.81	36.75			0.45	0.47	5.56	2.86	0.49	0.23	2.75	1.32	55.56	24.71
Spectrum 4 Compound 4: Ni, O, Mn with F	8.5	18.07	24.26	38.71	14.7	19.75	0.29	0.28	13.23	6.15	4.44	1.92	34.36	14.94		
Spectrum 5 Compound 5: Mn and O with Al	9.2	17.35	37.15	52.58	3.81	4.54	11.71	9.83	34.42	14.19			2.14	0.82	1.3.6	0.48

A comparison of the systematic analysis of the EDSX data shown in Figures 20–22, 25 and 26 (pristine cathode, upper and lower cathode of module 30, and upper and lower cathode of module 11) is shown below (Table 9).

Table 9. Comparison of the systematic analysis of the EDX data of the different cathodes analyzed.

CATHODE	Compound 1	Compound 2	Compound 3	Compound 4	Compound 5	Comments
Pristine Cathode	LiNiMnCoO$_2$	LMO + F				1. Compound 1 is the chemistry of a NMC cathode 2. Compound 2 is an LMO, and the F may be from the electrolyte (LiPF6) in contact with the cathode and anode.
Upper Cathode of Module 30	Mn and O, with some F and P	F and Ni				1. Compound 2 is due to the reactions in the TR, and is why there are leftovers of the electrolyte.
Lower Cathode of Module 30	O and Mn	O and Ni with some Mn, F, Co, and Al				1. Aluminum of compound 2 comes from the fusion of the cathode aluminum collector.
Upper Cathode of Module 11	C and O	O and Al	C, O, Mn, Co, and Ni, with some Al			1. Compound 2 is formed from the fusion of the cathode aluminum collector. 2. The aluminum of compound 3 comes from the fusion of the cathode aluminum collector.
Lower Cathode of Module 11	Ni, Mn, O, C, Co with Al and Cu	Ni, Mn, C, Co and O	Cu and O	Ni, O, Mn with F	Mn and O with Al	1. Compound 1 presents all the elements of the cathode coating; the copper may come from the anode collector. 2. Compound 3 has probably been formed because the anode collector has melted. 3. Compound 4 has F due to the reactions in the TR and why there are leftovers of the electrolyte. 4. Compound 5 is formed from the active material of the cathode, and there is also aluminum from the aluminum collector of the cathode.

After carrying out the comparative analysis presented in Table 9, it can be concluded that the cathodes of the ignited modules present compounds containing the elements of the cathode coating. However, they also present in some areas aluminum from the melting of the aluminum collector of the cathode, as well as copper from the melting of the copper collector of the anode. There are also traces of fluorine from the electrolyte (LiPF6). Copper only appears on the lower cathode of module 11, and more compounds appear, so it can be concluded that this is the most damaged cathode analyzed.

The following images (Figure 27) compare different images obtained with FESEM of the upper anode of module 30, module 11, and the new cell. And in Figure 28, different images obtained with FESEM of the lower anode of module 30, module 11, and the new cell are compared.
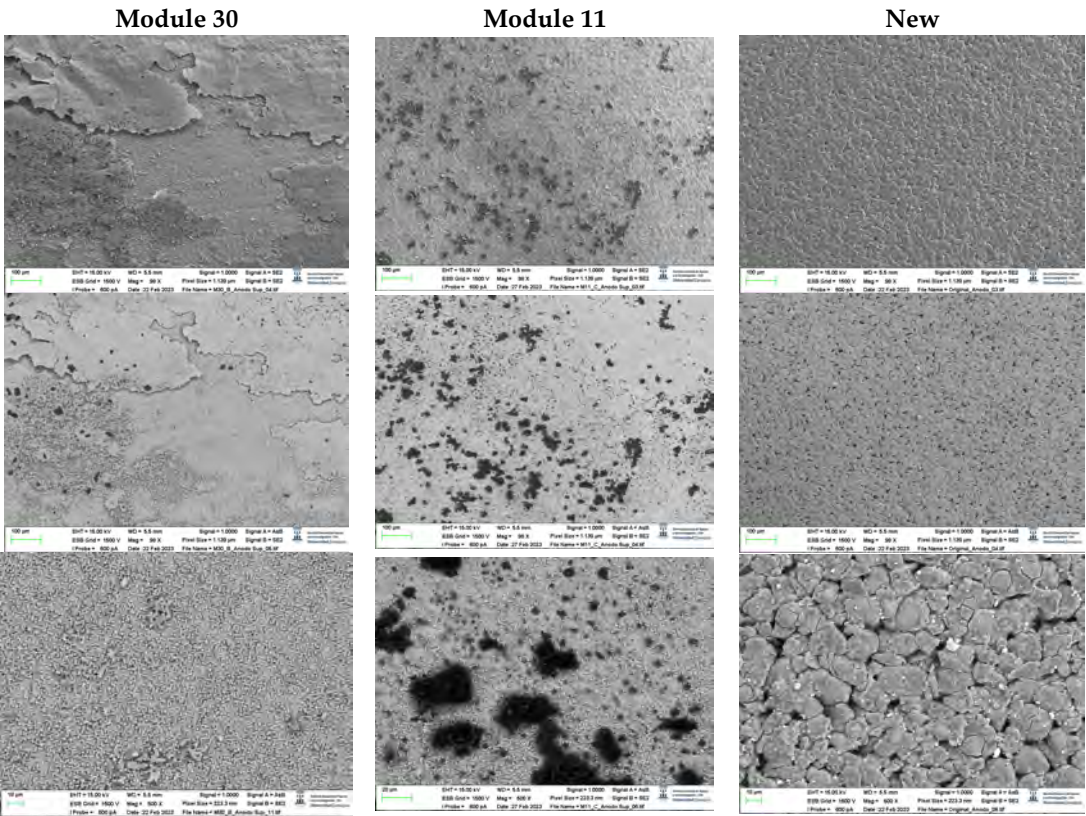
Module 30 **Module 11** **New**

Figure 27. Comparison of images obtained with the FESEM of different areas of the upper anode of module 30, module 11, and the new cell.

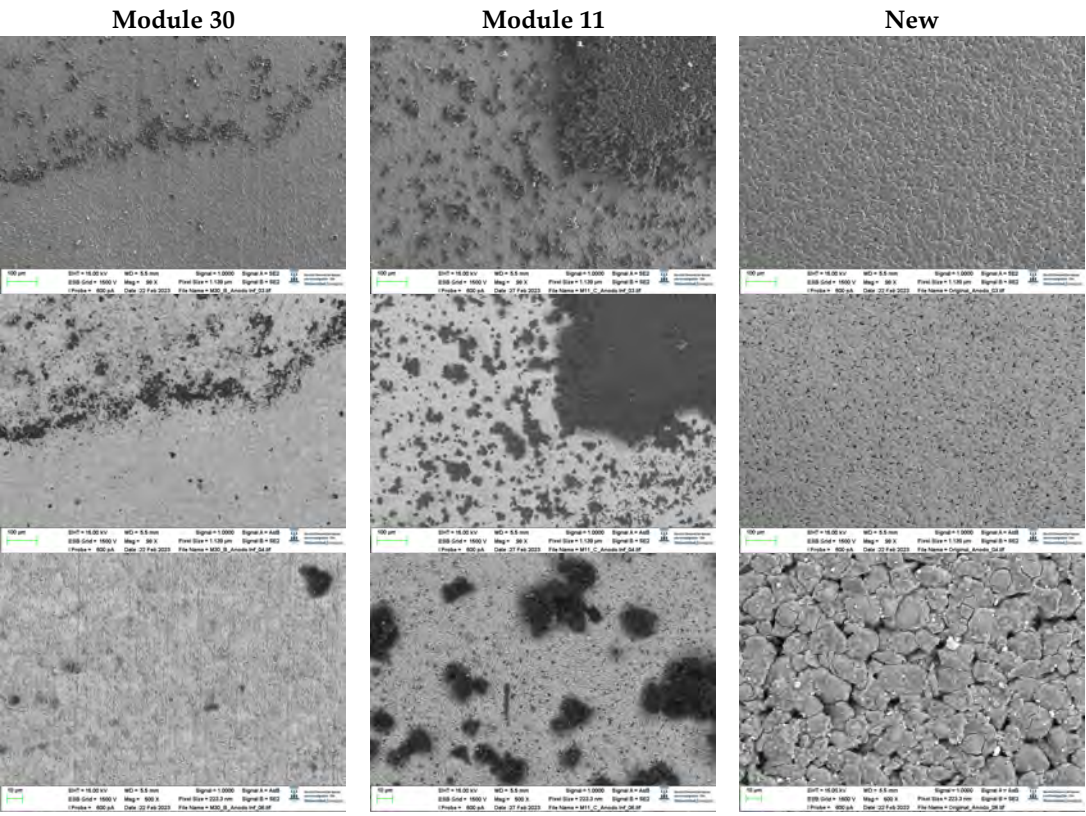**Module 30** **Module 11** **New**

Figure 28. Comparison of images obtained with the FESEM of different areas of the lower node of module 30, module 11, and the new cell.

With respect to the anode electrodes in the previous figure, as it has been done with the cathode electrodes, the anode of an original cell with two anodes (one upper and one lower) was compared with module 30 and module 11 of the battery of the burning Nissan Leaf, i.e., after experiencing the thermal runaway. It is observed that after experiencing the thermal runaway, spherical particles exist on the graphite anode surface. These spherical surfaces are covered with smaller stereoscopic particles, as can be seen in Figures 28 and 29.

The original graphite anode has a porous structure that disappears when it undergoes a TR because the pores are occupied by spherical particles. When TR happens, the exothermic reaction on the anode side is linked to the creation of stereoscopic particles. However, at higher temperatures, Li_2CO_3 can be formed by the reaction of the intercalated carbon with the electrolytes [31], since at a temperature above 120 °C, the SEI decomposes. In addition, as the temperature increases, at approximately 290 °C, the lithited carbon could react with fluorine to form LiF [31].

After the analysis of the cathode and anode states after experiencing the TR, it is concluded that the spherical structure of the cathode active materials and the flake structure of the graphite are destroyed. It was quite difficult to obtain the sample from the ignited modules to identify them due to the fact that the cathode and anode were joined together.

It is observed that there are many impurities, not regular in shape, on the surface of the electrode. Sometimes it is rectangular, and sometimes it is spherical. The surface distribution is chaotic, as can be seen in Figure 29b,c. Because the temperature at which TR is reached in NMC pouch cells is high, the aluminum current collector of the cathode is oxidized and bonded to the anode. Therefore, it is normal to identify debris in the image observed with the SEM. Studies [30] indicate that this debris can be fragments of cathode materials, separator and cathode ash, products of exothermic reactions, as well as graphite flaking. In some areas, a dense and brittle layer has been found on the surface of the electrode. In other areas, flake graphite particles were found under this layer. Thus, it follows that this layer was an oxidized aluminum current collector. Unlike in the cathode, the pores of the anode have been clogged by materials from TR reactions. In some areas, a dense, brittle layer covering the surface of the electrode is also observed. In other areas, flake graphite particles were observed under this layer. Therefore, the authors contemplated that this layer was an oxidized Al current collector. Judging by the structure of the base layer, it was the layer of active material on the anode. Unlike the active material coating of the cathode of new cells, the pores of the electrode that suffered thermal runaway had been completely clogged by the products of the thermal runaway reactions. The active material of the cathode had completely ceased to function. If the structural transformation (morphology analysis with InLens) of the anode materials after the TR is analyzed (Figures 30 and 31), it is observed that in the case of modules 30 and 11 with a SoC at 68% after the TR, the layered structure of the material was destroyed, the particles dispersed outside the original layered structure and adhesion occurred. The cathode (positive electrode) material reacted at high temperatures and decomposed. On the other hand, carbon particles from the anode (negative electrode) went into the positive electrode (cathode) structure through the damaged diaphragm.
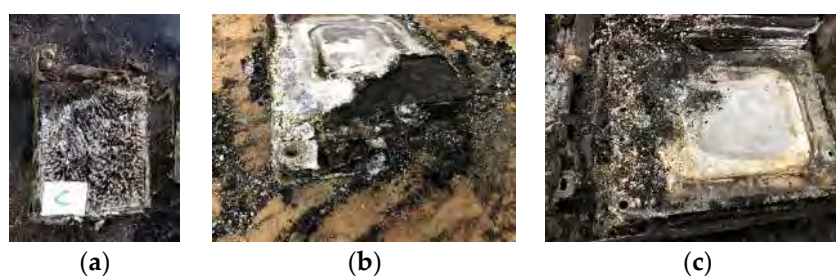

Figure 29. (**a**) Cell c of module 30; (**b**) Module 11 set on fire; (**c**) Module 30 burned down.

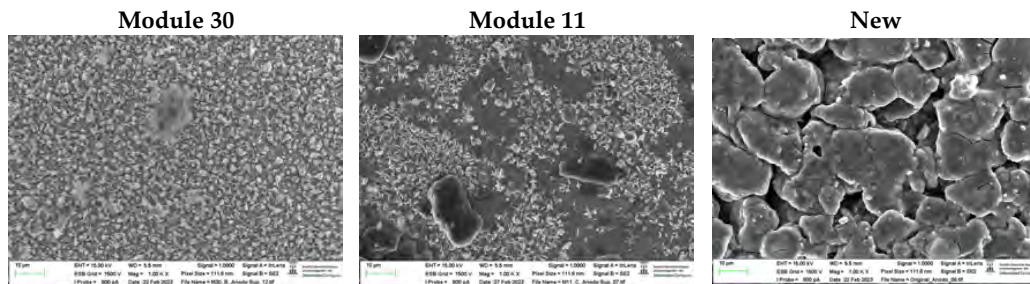| Module 30	Module 11	New

Figure 30. Morphological analysis of the transformation of the upper anode of module 30 and module 11 after the thermal runaway compared with the initial anode structure of a new cell.
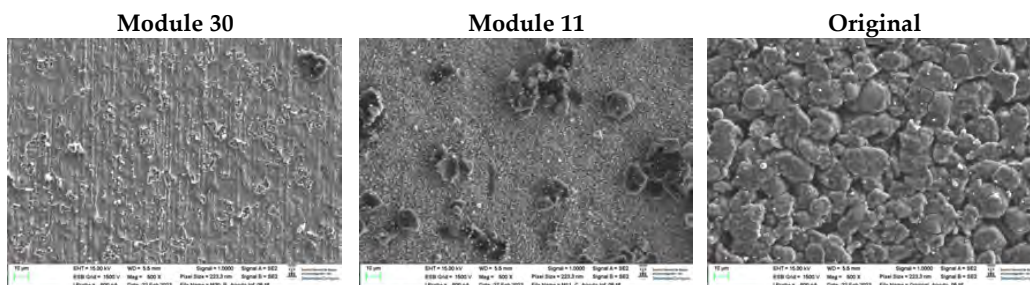
Module 30	Module 11	Original

Figure 31. Morphological analysis of the transformation of the lower anode of module 30 and module 11 after the thermal runaway compared with the initial anode structure of a new cell.

The chemical composition of the new cell anode is then analyzed. The anode has a granular structure. The diameter of the largest particles was 14 µm. Four types of zones are identified, where the chemical elements will be analyzed. The chemical analysis revealed a high content in zone 2 of carbon (C), which allows the active material of the anode to be identified as graphite. There are traces of phosphorus (P) that can be identified as remnants of the electrolyte (assumed that it is LiPF6 dissolved in a carbonate mixture solvent). Also, in zone 1, a fluorine peak is identified; it can be seen on the surface of the graphite particles and can be attributed to the decomposition of the electrolyte that is part of the SEI. The small peaks of Cu can be attributed to the preparation of the sample and can be neglected. On the other hand, in zones three and four, peaks of calcium and iron are identified due to the shape of which impurities can be considered to have appeared due to the preparation of the sample. Manganese also appears.

Details of the four spectra of the component values measured in atomic and weight % in the original anode (Figure 32) are listed in Tables 10 and 11.
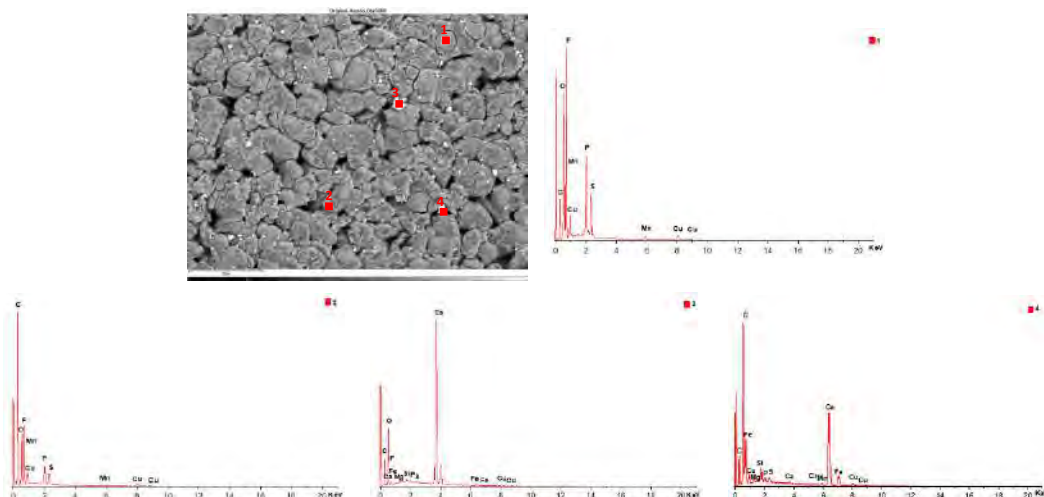

Figure 32. Chemical composition of the new cell anode.

Table 10. EDXS weight ratio of components in the original anode using the first two spectra focused on two distinct areas.

	C		O		F		P		S		Mn		Cu	
	Weight (%)	Atomic (%)	Weight (%)	Atomic (%)	Weight (%)	Atomic (%)	Weight (%)	Atomic (%)	Weight (%)	Atomic (%)	Weight (%)	Atomic (%)	Weight (%)	Atomic (%)
Spectrum 1 Compound 1: C, O, F and P	17.9	27.54	21.36	24.67	37.97	36.93	8.55	5.1	5.31	3.06	2.14	0.72	6.77	1.97
Spectrum 2 Compound 2: C, O, F with P	56.04	67.86	16.53	15.03	18.19	13.92	2.64	1.24	1.84	0.83	0.86	0.23	3.91	0.89

Table 11. EDXS weight ratio of components in the original anode using the last two spectra focused on two distinct areas.

	C		O		F		Mg		Si		Ca		Fe		Cu	
	Weight (%)	Atomic (%)	Weight (%)	Atomic (%)	Weight (%)	Atomic (%)	Weight (%)	Atomic (%)	Weight (%)	Atomic (%)	Weight (%)	Atomic (%)	Weight (%)	Atomic (%)	Weight (%)	Atomic (%)
Spectrum 3 Compound 3: O, Ca and C	7.4	14.33	35.64	51.81	0.89	1.08	0.56	0.53	0.46	0.38	53.72	31.17	0.94	0.39		
Spectrum 4 Compound 4: C, O, Fe with F	10.61	25.37	20.01	35.94	1.62	2.44	0.58	0.69	1.35	1.38	0.42	0.3	60.39	31.07	2.8	1.27

The following Figure 33, shows the chemical composition of other compounds identified in the original anode. Zone 1 identifies a chemical compound of manganese and oxygen, and zone 2 identifies a chemical compound of carbon and oxygen with fluorine and phosphorus, which may be due to electrolyte, copper, and sulfur (the latter two elements may be due to impurities from sample preparation). The manganese in structure 1 may come from the manganese-based cathode because of the possibility of manganese ions intercalating along with lithium ions into graphite in the initial stage of the lithium-ion intercalation process during storage [37].
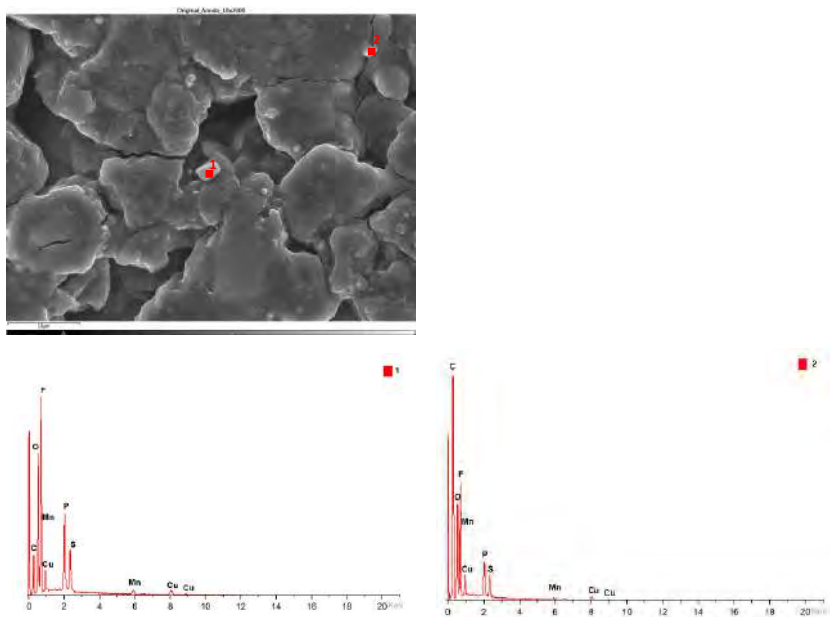

Figure 33. Chemical composition of the new cell anode 2.

Details of the two spectra of the component values measured in atomic and weight % in the original anode (Figure 33) are listed in Tables 12 and 13, respectively.

Table 12. EDXS weight ratio of components in the original anode using first spectrum focused area one.

	C		O		F		Al		P		Mn		Cu	
	Weight (%)	Atomic (%)	Weight (%)	Atomic (%)	Weight (%)	Atomic (%)	Weight (%)	Atomic (%)	Weight (%)	Atomic (%)	Weight (%)	Atomic (%)	Weight (%)	Atomic (%)
Spectrum 1 Compound 5: Mn and O	6.69	14.5	31.1	50.57	5.27	7.22	1.15	1.11	0.47	0.39	53.59	25.38	1.45	0.59

Table 13. EDXS weight ratio of components in the original anode using second spectrum focused area two.

	C		O		F		Si		P		S		Mn		Cu	
	Weight (%)	Atomic (%)	Weight (%)	Atomic (%)	Weight (%)	Atomic (%)	Weight (%)	Atomic (%)	Weight (%)	Atomic (%)	Weight (%)	Atomic (%)	Weight (%)	Atomic (%)	Weight (%)	Atomic (%)
Spectrum 2 Compound 6: C and O with F and P, Cu and S	37.83	51.52	23.87	24.41	19.17	16.51	1.78	1.04	3.4	1.8	2.98	1.52	0.92	0.27	8.8	2.27

Afterward, the chemical composition of the upper anode of the ignited module 30 is analyzed. The upper anode of module 30 also does not show a defined granular surface, as in the case of the original anode; the structure was broken. Two different types of compounds were observed on the surface of the upper anode of module 30, shown in Figure 34. A detailed analysis of the compounds formed shows that the compound marked with "2" had the chemical of a copper and oxygen compound, which may be due to the anode collector having melted due to the elevated temperatures; moreover, while zone 3 was a carbon and oxygen compound, it may be due to the coating of the graphite anode.
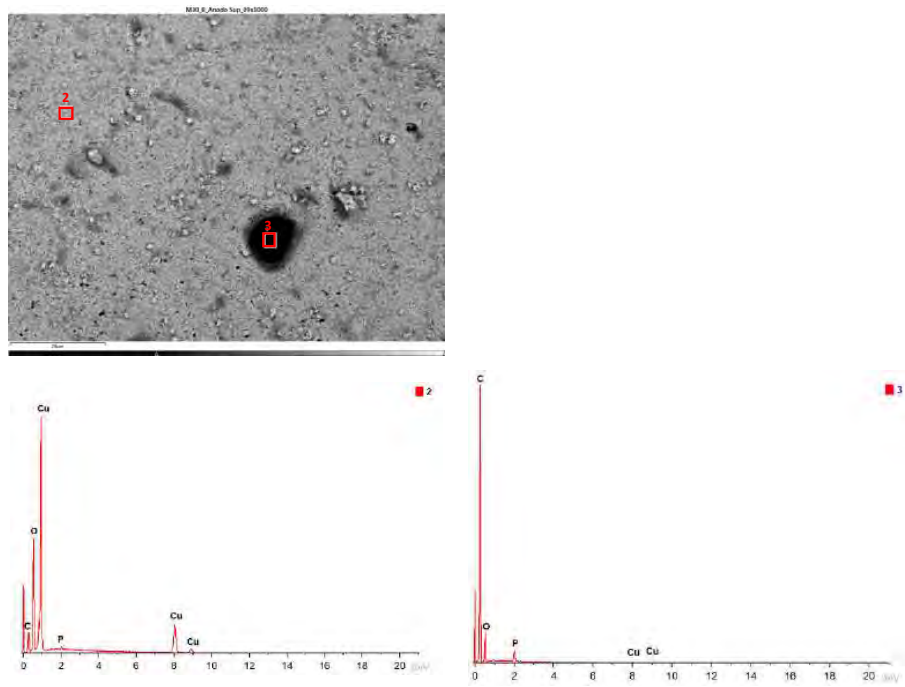

Figure 34. Chemical composition of the upper anode of module 30.

As has been performed previously, details of the two spectra of the component values measured in atomic and weight % in the upper anode of module 30 (Figure 34) are listed in Table 14.

Table 14. EDXS weight ratio of components in the upper anode of the ignited module 30 using two spectra focused on two distinct areas.

		C		O		F		P		Cu	
		Weight (%)	Atomic (%)	Weight (%)	Atomic (%)	Weight (%)	Atomic (%)	Weight (%)	Atomic (%)	Weight (%)	Atomic (%)
Compound 1: Cu and O	Spectrum 2	12.44	29.63	22.9	40.97			0.58	0.54	64.08	28.86
Compound 2: C and O	Spectrum 3	80.31	85.45	16.39	13.09	0.82	0.55	1.93	0.8	0.55	0.11

In Figure 35 below, the chemical composition in another area of the upper anode of the ignited module 30 is analyzed. A single type of compound was observed on the surface of the upper anode of module 30. This compound features copper, carbon, and oxygen.
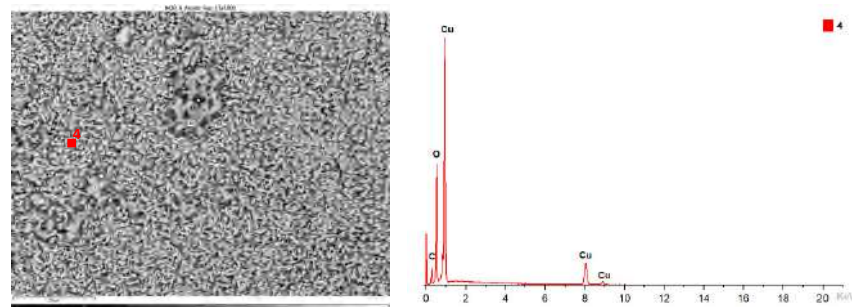

Figure 35. Chemical composition of the upper anode of module 30, second area analyzed.

Details of the one spectrum of the component values measured in atomic and weight % in the upper anode of module 30 (Figure 35) are listed in Table 15.

Table 15. EDXS weight ratio of components in the upper anode of the ignited module 30 using one spectrum-focused area four.

		C		O		Cu	
		Weight (%)	Atomic (%)	Weight (%)	Atomic (%)	Weight (%)	Atomic (%)
Compound 3: Cu, C and O	Spectrum 4	10.15	25.18	23.45	43.67	66.4	31.14

In Figure 36 below, the chemical composition in another area of the upper anode of the ignited module 30 is analyzed. Four different types of compounds were observed. In the first two ones, a compound of copper, carbon, and oxygen was observed. In zone 3, fluoride, copper, and oxygen were identified; the existence of fluoride is due to the electrolyte, and the existence of copper is due to copper from the anode collector. In zone 4, cooper and oxygen were identified.
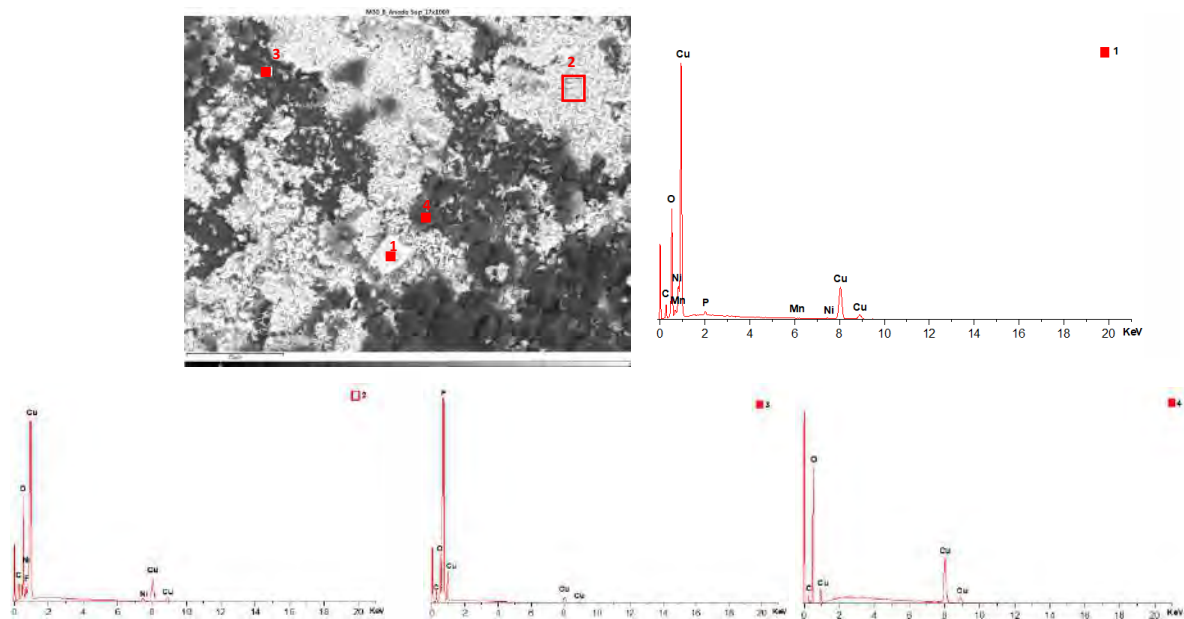
Figure 36. Chemical composition of the upper anode of module 30, third area analyzed.

As has been performed previously, details of the four spectra of the component values measured in atomic and weight % in the upper anode of module 30 (Figure 36) are listed in Table 16.

Table 16. EDXS weight ratio of components in the upper anode of the ignited module 30 using five spectra focused on five distinct areas.

	C		O		F		P		Mn		Ni		Cu	
	Weight (%)	Atomic (%)	Weight (%)	Atomic (%)	Weight (%)	Atomic (%)	Weight (%)	Atomic (%)	Weight (%)	Atomic (%)	Weight (%)	Atomic (%)	Weight (%)	Atomic (%)
Spectrum 1 Compound 3: Cu, C and O	8.8	23.11	21.12	41.67			0.63	0.65	0.36	0.21	1.1	0.59	67.98	33.77
Spectrum 2 Compound 3: Cu, C and O	11.2	26.72	22.2	39.69	3.28	4.95					4.02	1.96	59.27	26.68
Spectrum 3 Compound 4: F, Cu and O	5.77	9.93	7.7	9.96	68.03	74.09							18.51	6.03
Spectrum 4 Compound 1: Cu and O	5.03	7.99	71.19	84.87									23.78	7.14

Next, the chemical composition of the lower anode of the ignited module 30 is analyzed. The lower anode of module 30 also does not show a defined granular surface, as in the case of the original anode; the structure was broken. Two different types of compounds were observed on the surface of the lower anode of module 30, shown in Figure 37. A detailed analysis of the compounds formed shows that the compound marked with "1" had the chemistry of a Carbon and oxygen compound, which may be due to the anode coating, and the second structure features copper, carbon, and oxygen.
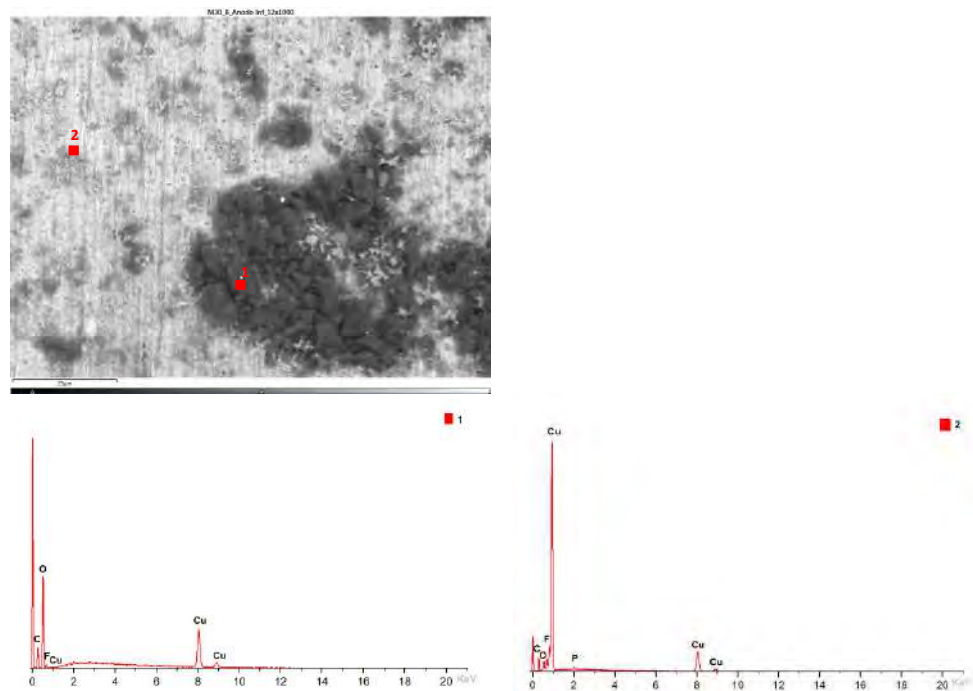
Figure 37. Chemical composition of the lower anode of module 30.

As has been performed previously, details of the two spectra of the component values measured in atomic and weight % in the lower anode of module 30 (Figure 37) are listed in Table 17.

Table 17. EDXS weight ratio of components in the lower anode of the ignited module 30 using two spectra focused on two distinct areas.

		C		O		F		P		Cu	
		Weight (%)	Atomic (%)	Weight (%)	Atomic (%)	Weight (%)	Atomic (%)	Weight (%)	Atomic (%)	Weight (%)	Atomic (%)
Compound 1: C and O with F	Spectrum 1	19.23	24.44	70.73	67.49	10.04	8.07				
Compound 2: Cu, C and O	Spectrum 2	15.55	45.38	2.89	6.34	2.29	4.22	0.56	0.63	78.71	43.42

Figure 38 below shows the chemical composition in another area of the upper anode of the ignited module 11. Six different types of compounds were observed on the surface of the upper anode of module 11. The compound marked with "1" is carbon, coming from the graphite of the anode coating; the compound marked with "2" is a compound of fluorine, copper, and oxygen; fluorine comes from the electrolyte; and the rest of the compounds have copper, carbon, and oxygen.
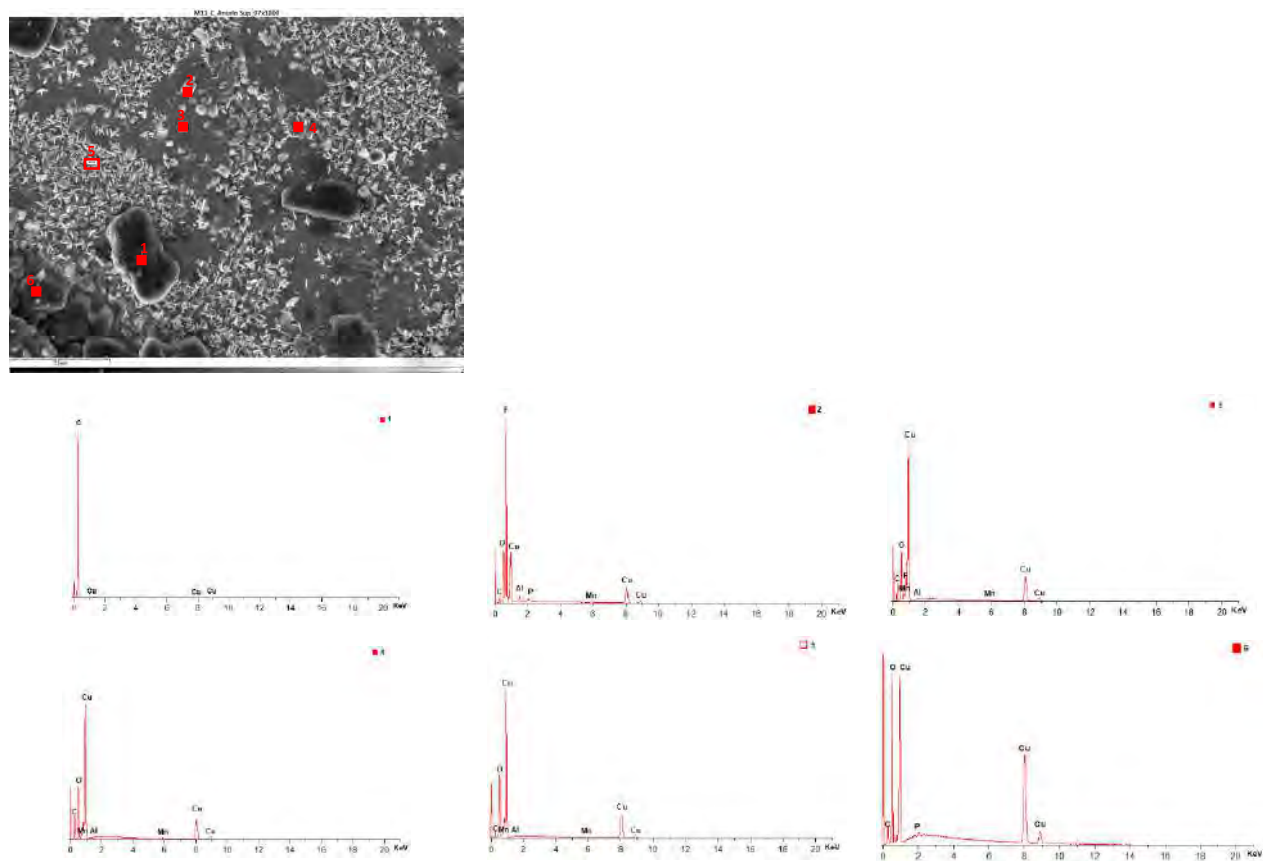
Figure 38. Chemical composition of the upper anode of module 11.

Details of the six spectra of the component values measured in atomic and weight % in the upper anode of module 11 (Figure 38) are listed in Table 18.

Table 18. EDXS weight ratio of components in the upper anode of ignited module 11 using six spectra focused on six distinct areas.

	C		O		F		Al		P		Mn		Cu	
	Weight (%)	Atomic (%)	Weight (%)	Atomic (%)	Weight (%)	Atomic (%)	Weight (%)	Atomic (%)	Weight (%)	Atomic (%)	Weight (%)	Atomic (%)	Weight (%)	Atomic (%)
Spectrum 1 Compound 1: C	100	100												
Spectrum 2 Compound 2: F, Cu and O	3.16	6.28	11.72	17.47	48.95	61.48	1.45	1.29	1.02	0.78	0.77	0.33	32.93	12.37
Spectrum 3 Compound 3: Cu, C and O	17.7	40.76	16.52	28.58	1.73	2.52	0.35	0.36			0.68	0.34	63.01	27.44
Spectrum 4 Compound 4: Cu, C and O	22.43	46.75	19.34	30.25							0.92	0.42	57.31	22.57
Spectrum 5 Compound 5: Cu, C and O	8.13	21.76	21.06	42.31							1.55	0.91	69.25	35.03
Spectrum 6 Compound 3: Cu, C and O	9.09	19.54	34.02	54.92	2.19	2.98			0.76	0.63			53.93	21.92

And finally, in the following Figure 39, the chemical composition in another area of the lower anode of the burning module 11 is analyzed. Six different types of compounds were observed on the surface of the lower anode of module 11. The first structure was a compound of fluorine, copper, and oxygen; in compound 2, copper and oxygen were identified; compound 3 is like the first, which is a compound of fluorine, copper and

oxygen. In compound 4 there is more copper than fluorine and oxygen, and in structures 5 and 6, there is copper oxide and carbon oxide.
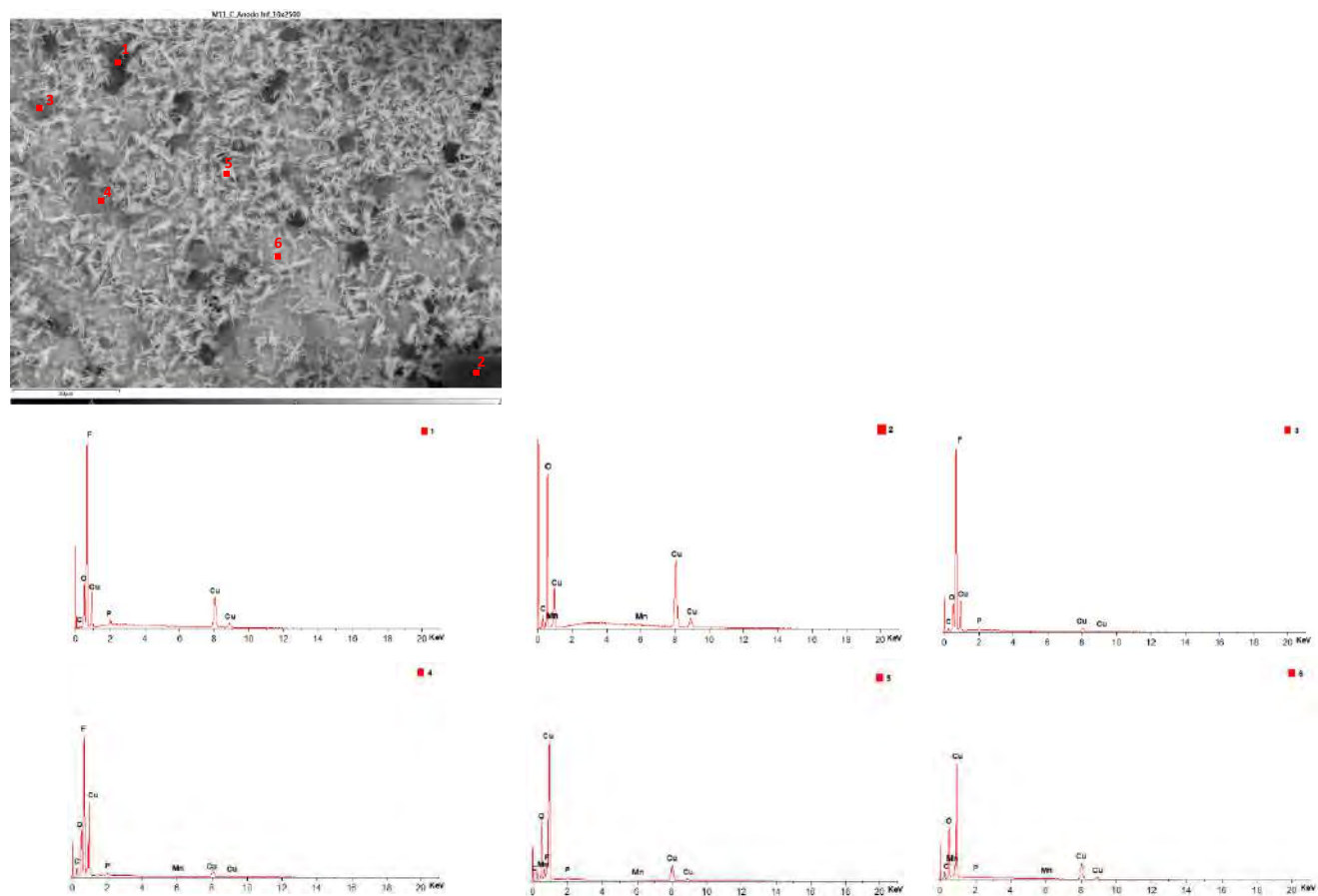

Figure 39. Chemical composition of the lower anode of module 11.

Details of the six spectra of the component values measured in atomic and weight % in the lower anode of module 11 (Figure 39) are listed in Table 19.

Table 19. EDXS weight ratio of components in the lower anode of ignited module 11 using six spectra focused on six distinct areas.

		C		O		F		P		Mn		Cu	
		Weight (%)	Atomic (%)	Weight (%)	Atomic (%)	Weight (%)	Atomic (%)	Weight (%)	Atomic (%)	Weight (%)	Atomic (%)	Weight (%)	Atomic (%)
Compound 1: F, Cu and O	Spectrum 1			11.27	16.76	56.01	70.15	2.12	1.63			30.6	11.46
Compound 2: Cu and O	Spectrum 2	9.43	16.41	54.94	71.73					2.98	1.13	32.65	10.73
Compound 1: F, Cu and O	Spectrum 3	3.02	5.83	8.14	11.78	58.17	70.9	0.83	0.62			29.84	10.87
Compound 1: F, Cu and O	Spectrum 4	7.66	15.87	11.24	17.48	37.6	49.28	0.71	0.57	0.41	0.18	42.39	16.61
Compound 3: Cu, C and O	Spectrum 5	10.03	25.01	20.16	37.73	3.81	6	0.2	0.2	0.79	0.43	65.01	30.63
Compound 3: Cu, C and O	Spectrum 6	10.49	26.3	22.19	41.76					0.56	0.31	66.76	31.63

The analysis of the cell anodes after the fire test shows that the anode has peaks of oxygen and peaks of carbon, which indicates the formation of lithium carbonate (Li_2CO_3).

A comparison of the systematic analysis of the EDSX data shown in Figures 32–39 (pristine anode, upper and lower anode of module 30, and upper and lower anode of module 11) is shown below (Table 20).

Table 20. Comparison of the systematic analysis of the EDX data of the different anodes analyzed.

ANODE	Compound 1	Compound 2	Compound 3	Compound 4	Compound 5	Compound 6	Comments
Pristine Anode	C, O, F with P	C, O, F with P	O, Ca, and C	C, O, Fe, with F	Mn and O	C and O with F and P, Cu, and S	1. The F of compound 1 can be attributed to the decomposition of the electrolyte. 2. The C of compound 2 allows the active material of the anode (graphite). The traces of P are remnants of the electrolyte ($LiPF_6$). 3. In compounds 3 and 4, there are Ca and Fe due to the preparation of the sample (impurities). 4. The Mn in compound 5 comes from the manganese-based cathode. 5. In compound 6, the traces of F and P may be due to electrolytes, and the traces of Cu and S may be due to the sample preparation (impurities).
Upper Anode of Module 30	Cu and O	C and O	Cu, C, and O	F, Cu, and O			1. Compound 1 may be due to the anode collector having melted due to elevated temperatures. 2. The compound 2 may be due to the coating of the graphite anode. 3. In the case of compound 3, it can come, on the one hand, from Cu due to the melting of the copper collector of the anode and, on the other hand, from C due to the coating of the graphite anode. 4. The existence of F in compound 4 is due to the electrolyte.
Lower Anode of Module 30	C and O with F	Cu, C, and O					1. The compound 1 may be due to the coating of the graphite anode. And the existence of F is due to the electrolyte. 2. In the case of compound 2, its elements can come, on the one hand, from Cu due to the melting of the copper collector of the anode, and on the other hand, C from the coating of the graphite anode.
Upper Anode of Module 11	C	F, Cu, and O	Cu, C, and O				1. Compound 1 is C, coming from graphite. 2. The existence of F in compound 2 is due to the electrolyte. And Cu comes from the melting of the copper collector of the anode. 3. In the case of compound 3, its elements can come, on the one hand, from Cu due to the melting of the copper collector of the anode, and on the other hand, C from the coating of the graphite anode.
Lower Anode of Module 11	F, Cu, and O	Cu and O	Cu, C, and O				1. The existence of F in compound 2 is due to electrolyte. And Cu comes from the melting of the copper collector of the anode. 2. In the case of compound 3, its elements can come, on the one hand, from Cu due to the melting of the copper collector of the anode and, on the other hand, from C due to the coating of the graphite anode.

After carrying out the comparative analysis presented in Table 20, it can be concluded that the anodes of the ignited modules present compounds containing the elements of the anode coating. However, they also present in some areas cooper from the melting of the cooper collector of the anode but no aluminum from the melting of the cathode collector. There are also traces of fluorine from the electrolyte ($LiPF_6$).

A morphological analysis of the separator of the new cell is then performed since the separator cannot be recovered in the burned modules because it has melted in the thermal runaway reaction. The surface structure of the separator was investigated to determine the thickness of the separator fibers and the size of the pores, as well as to determine whether an alumina layer had been deposited on the separator membrane, as described above. Figure 40 shows the results of the SEM image. The structure of the fibers of the polypropylene membrane $(C_3H_6)_n$ is shown on the right. The separator fibers were aligned perpendicular to the cell tabs.
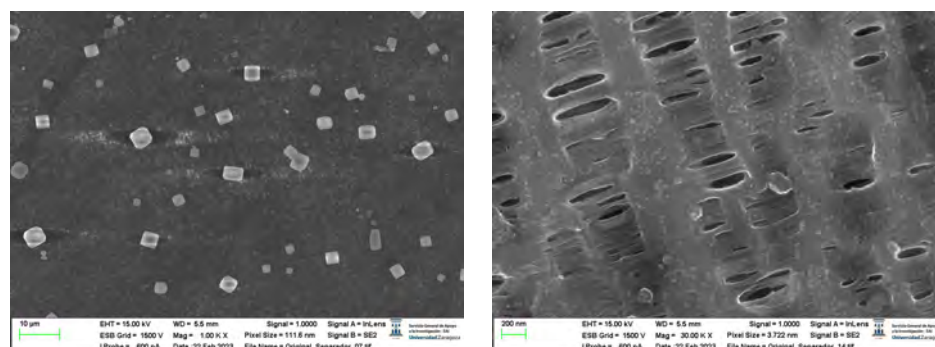
Figure 40. Morphological analysis of the separator. The first image has been obtained with a magnification of 1.00 K X, and the second image with a magnification of 30.00 K X.

The total thickness of the separating fiber was about 289 nm, as shown in Figure 41. The analyzed structure shows pores of different diameters, the smallest of about 41.61 nm and the largest of about 88.78 nm. The pore size in lithium-ion cells must be in the submicron range; it is a general requirement to prevent dendritic penetration of lithium from occurring over the life of the battery [38].
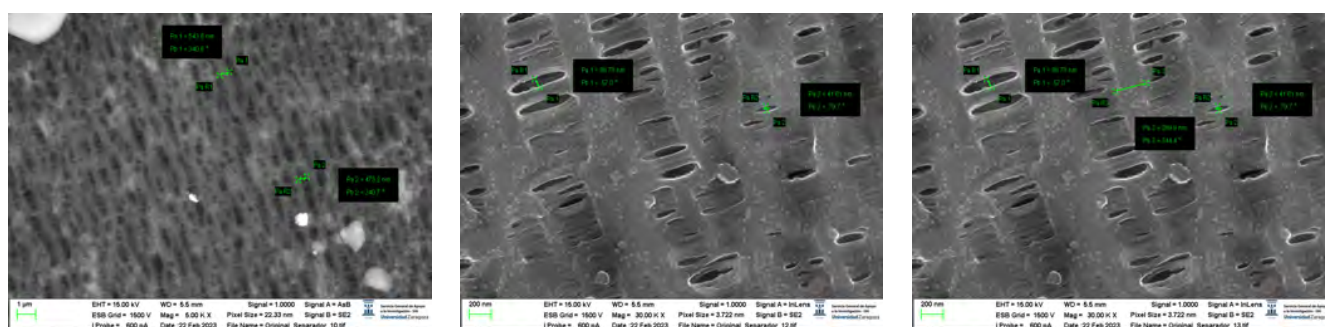
Figure 41. Morphological analysis of the separator. Measurement.

After that, the analysis of the separator's chemical composition will be performed. There are three types of compounds, the first being carbon with fluorine and phosphorus. The carbon is from the structure of the polypropylene separator itself; the fluorine and the phosphorus come from the electrolyte ($LiPF_6$) with which it is soaked. Compounds 2 and 3 have the same composition as the first compound.

As has been performed previously, details of the three spectra of the component values measured in atomic and weight % in the separator (Figure 42) are listed in Table 19.
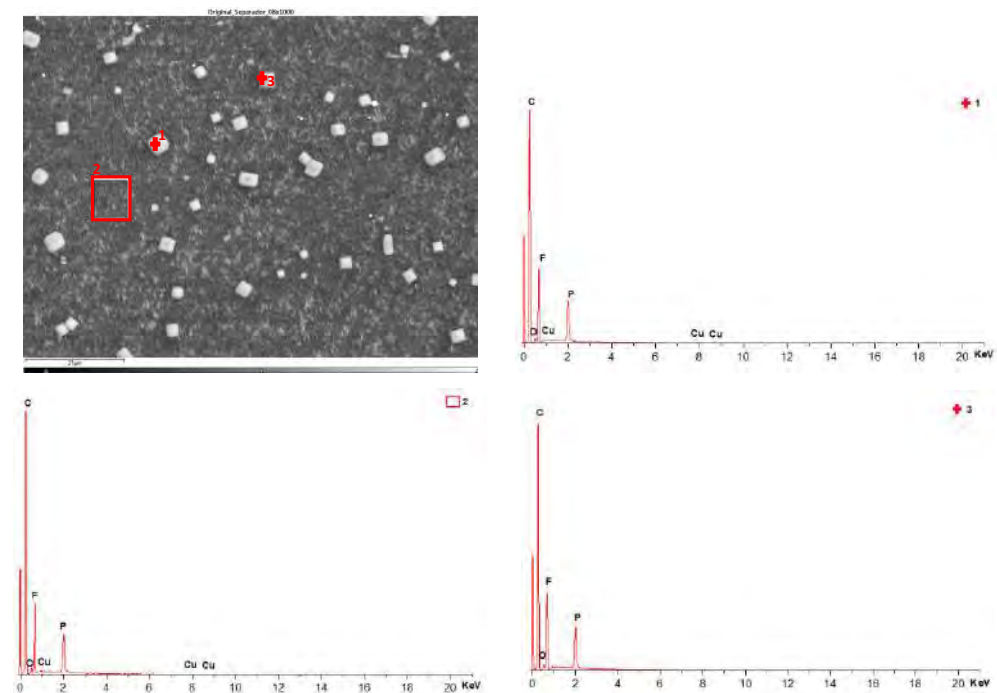
Figure 42. Chemical composition of the separator.

Details of the three spectra of the component values measured in atomic and weight % in the separator (Figure 42) are listed in Table 21.

Table 21. EDXS weight ratio of components in the separator using three spectra focused on three distinct areas.

	C		O		F		P		Cu	
	Weight (%)	Atomic (%)	Weight (%)	Atomic (%)	Weight (%)	Atomic (%)	Weight (%)	Atomic (%)	Weight (%)	Atomic (%)
Spectrum 1	81.14	71.43	1.57	1.84	14.57	20.29	2.61	5.94	0.11	0.51
Spectrum 2	83.58	74.96	1.87	2.24	12.39	17.59	2.07	4.79	0.09	0.42
Spectrum 3	81.16	71.74	1.73	2.03	14.49	20.26	2.61	5.96		

The layered structure was destroyed when the thermal runaway occurred. In the battery sample with a 68% SoC, there were characteristic fluoride peaks, indicating that after decomposition, the cathode material reacts with the electrolyte [39]. Characteristic carbon peaks are also shown; this is because, in the thermal runaway reaction, some of the carbon dust went into the positive electrode (cathode) material through the broken diaphragm [40]. It is observed that in the samples of module 11 and module 30, in which a thermal runaway reaction has occurred, the structure of the positive electrode (cathode) sample is destroyed, the particles were dispersed outside the original stratified structure, and the adhesion phenomenon occurred, indicating fragmentation. Particles are not found, and external impurities are placed in the structure [41].

The battery that caught fire in the test had a 68% SoC. Some studies [36] indicate that in the case of NMC batteries, the increase in SoC makes the thermal runaway reaction more intense, the temperature at which the thermal runaway starts is decreased, and the structural damage to the electrode materials is strong. In high-temperature conditions, the internal diaphragm of the battery is damaged, causing the battery to short circuit and worsen the thermal runaway reaction. During the thermal runaway reaction, the structure of the positive electrode (anode) material is destroyed, and the particles are dispersed outside the structure and adhere to the negative electrode (cathode).

If the particle size distribution (PSD) is compared for the case of the new cell and the burnt cells, it is observed that in the case of the latter, the particles of the positive electrode or cathode are smaller; they are further apart to facilitate the passage of gases and this gap will be occupied by another particle. In the case of burning cells, the particles are much smaller than in the case of new cells. Heat generation depends on the surface area and particle size of the positive electrode or cathode. There are studies [42] that show that the microstructure of particles can influence exothermic reactions of exothermic degradation.

3.2. Structural Test Results: Layer Properties of the Cell and Identification of Cell Details

In this section, the transversal-section investigation of the cells will be carried out, which will allow information about the structure and manufacture of the cells to be obtained, and the thickness measurement of each of the layers of the cell will be carried out.

The stacking of the different layers of the cell will be analyzed in the transversal section, which will allow us to identify interesting fabrication details of the pouch cells. First, the sample taken from zone 3 (Figure 12a) is analyzed, the central area on the opposite side to the area where the battery tabs of the cell are (Figure 43).
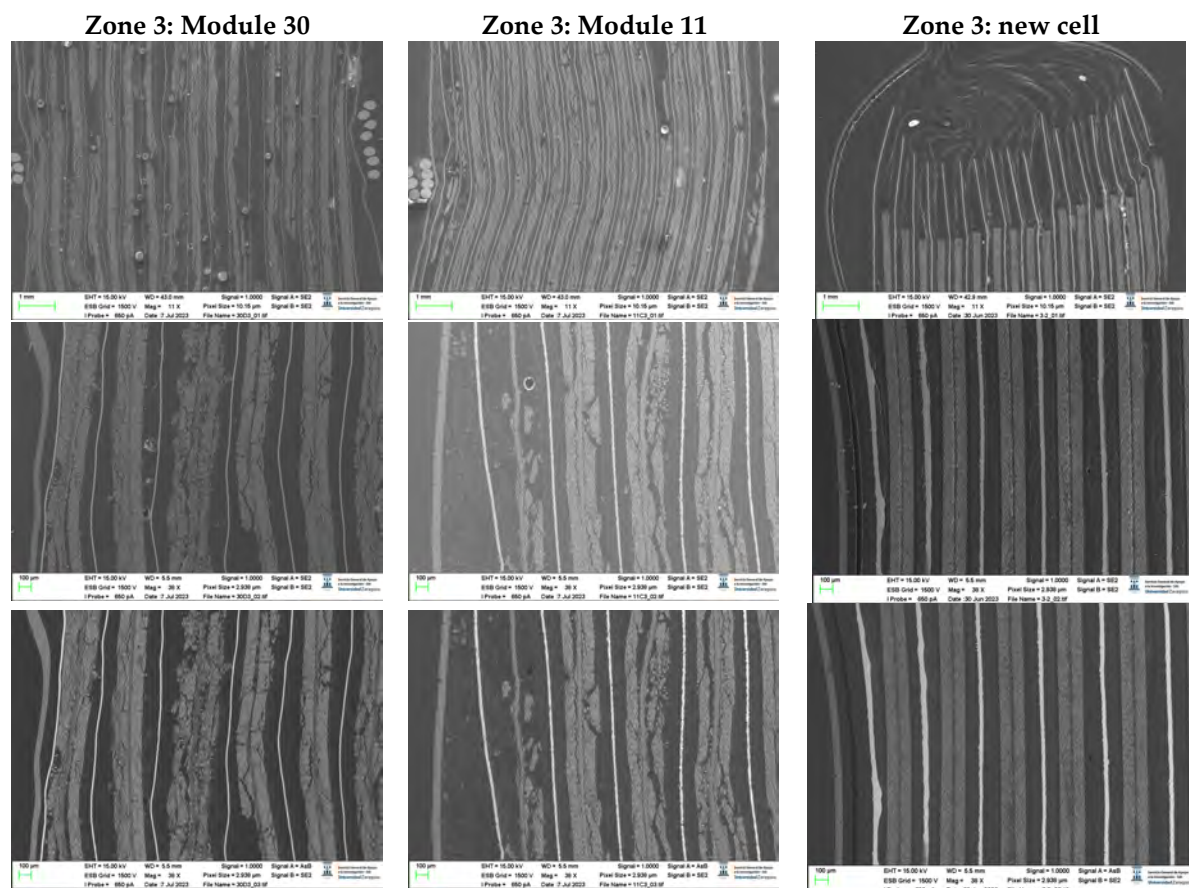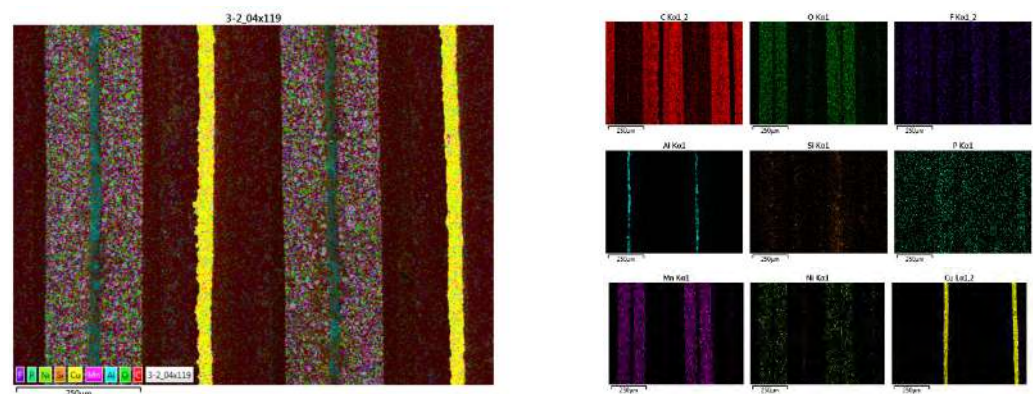

Figure 43. Images of the section of the pouch cell in zone 3 (central area on the opposite side to the one where the battery tabs of the cell are located Figure 12a).

It is observed that all the separating membranes are welded to the bag in a sealing point near the edge. Regarding the mechanical behavior of the cell and its possible failure, this fact indicates that when mechanical forces are applied to the battery near this axis, the separator may experience high tensile loads, and mechanical rupture of the separator membrane may occur. This would cause the battery electrodes to come into contact, which is the prerequisite for experiencing an electrical failure and thermal runaway. It is noticed that near the battery edge, the distances between layers become smaller due to the hot-

welded area of the bag. Since there are no layers in this part of the battery, a short circuit will not occur even if some of the battery layers are too close to each other.

Another purpose of an anode layer that is longer than the cathode is to increase the battery rigidity near the edge, which smooths the distribution of charge in the event of charging at the edge. The investigated cell contained 18 anodic layers, 17 cathode layers, and 34 separator sheets. The electrodes on both sides of the battery were anodes. This observation indicates that the active material deposited outside the last copper foil remained electrochemically inactive and, therefore, did not participate in the energy storage or charge transfer process.

In lithium-ion batteries, a layer of aluminum oxide (Al_2O_3) is usually deposited on the separator membrane to improve its thermal resistance as well as its thermal properties.

If the morphology is analyzed, it can be concluded that the outer area of zone three is more damaged in the case of module 11, while in the case of module 30, the central area is more damaged. It is also observed that the thickness of the copper collector decreases in case of thermal runaway, and it is observed to be narrower for module 30. To know the chemical composition of zone 3 in the original cell, a map of the distribution of elements was made (Figure 44). The copper collector (yellow) and the aluminum collector (blue) are identified. The coating of the anode is also observed, which is made of graphite (carbon, red color) and the coating of the cathode (composed of oxygen, manganese, and nickel). Electrolyte fluoride is also observed.

Figure 44. Distribution of the elements of a new pouch cell in zone 3 (central area on the opposite side to the one where the battery tabs of the cell are located).

After that, the chemical composition of zone 3 was analyzed for the case of the cell of the burned module 30.

Figure 45d shows the structure of the pouch cell of the burned module 30 in zone 3, three zones have been marked with a green box in which the composition of each of the layers of this pouch cell will be analyzed (Figure 45a–c). Figure 45a identifies the pouch of the pouch cell, which is made of aluminum (zones 2 and 3). In zone 5, there is carbon that may be graphite from the anode coating. Figure 46c identifies the cathode (manganese nickel oxide), and there are also carbon particles. Around the aluminum manifold, alumina (Al_2O_3) has been deposited on the separator in the cathode area. Alumina (aluminum oxide) has been deposited. In Figure 45b, the anode area has been detected, as well as graphite (carbon) coating and a layer with copper, oxygen, and the anode collector shell.

Moreover, the chemical composition of zone 3 (Figure 12a) is analyzed in the case of the cell of the burning module 11.

Figure 46d shows the structure of the pouch cell of the burned module 11 in zone 3, three zones have been marked with a green box in which the composition of each of the layers of this pouch cell will be analyzed (Figure 46a–c).
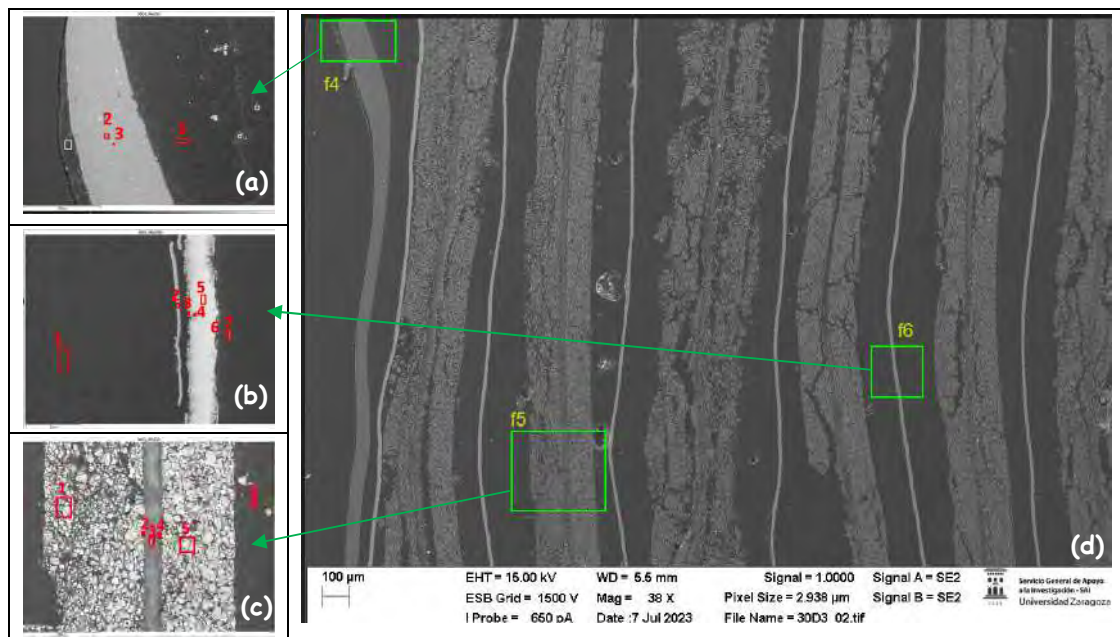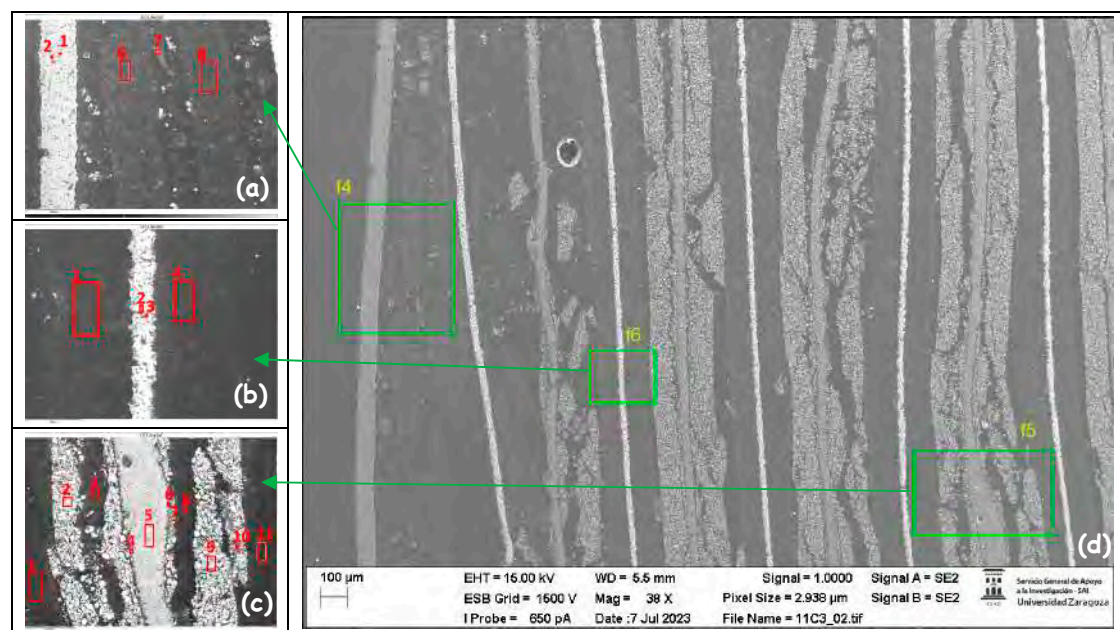
Figure 45. Chemical composition of each of the layers of the pouch cell of module 30 in zone 3 (central zone on the opposite side to that of the battery tabs of the cell Figure 12a).

Figure 46a identifies the pouch of the pouch cell, which is made of aluminum (zones 1 and 2); it appears more damaged than the bag of module 30. In zones 6 and 8, there is a compound of carbon and oxygen with some fluorine from the electrolyte, and in zone 7, there is a compound of carbon and oxygen with aluminum from the cathode collector. Figure 46c identifies the cathode (manganese oxide), and there are also carbon particles. In this case, aluminum is not observed. In Figure 46b, the anode zone has been detected. Then, there is a copper layer and a copper collector. Lastly, there are silicon particles, and a graphite coating layer is detected. The silicon particles could be due to traces of a sealant material.

Figure 46. Chemical composition of each of the layers of the pouch cell of module 11 in zone 3 (central zone on the opposite side to that of the battery tabs of the cell Figure 12a).

The sample obtained in zone 1 (anode battery tabs) (Figure 12a) is analyzed below (Figure 47):

Zone 1: Module 30	Zone 1: Module 30	Zone 1: new cell
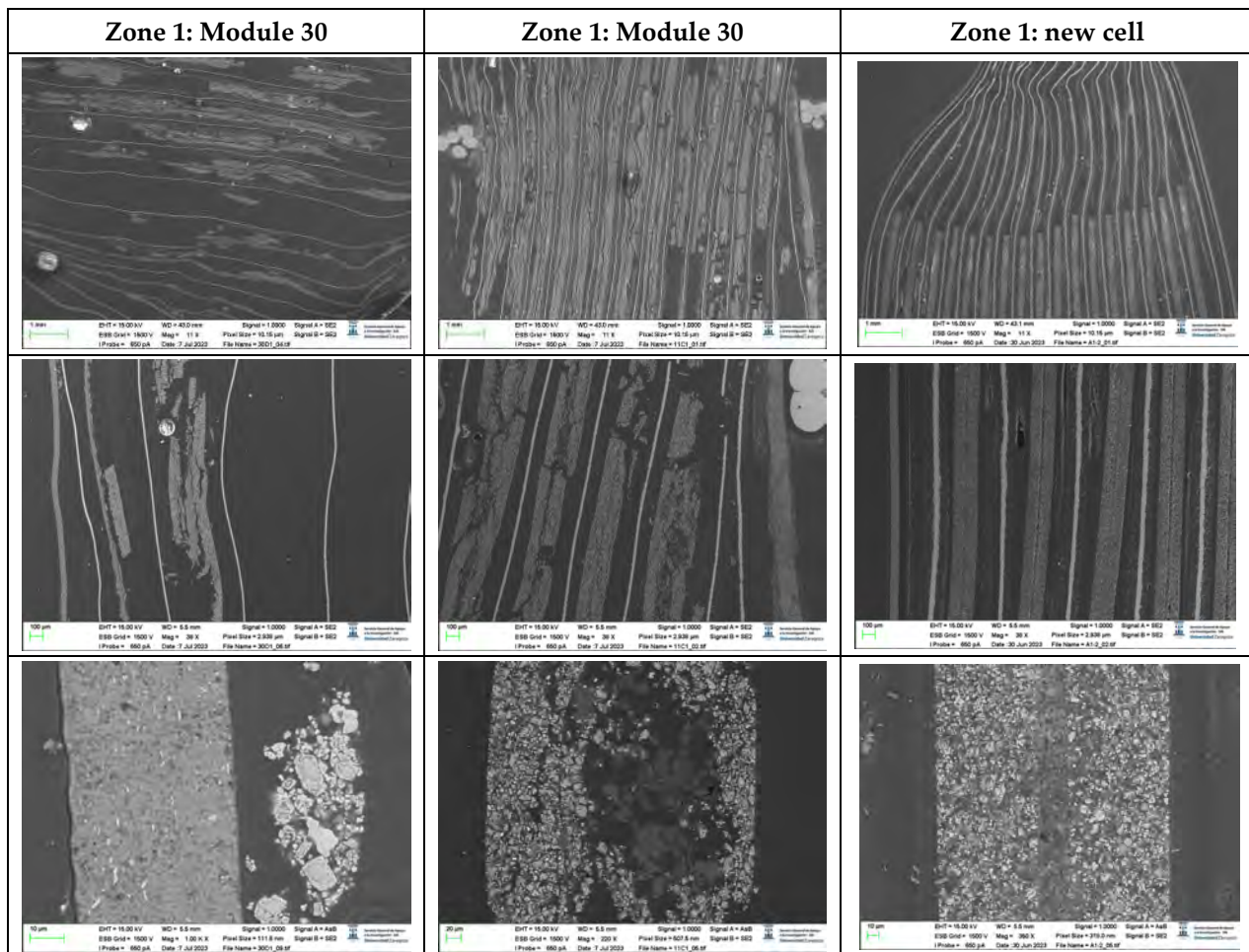
Figure 47. Images of the pouch cell section in zone one (anode zone) of the cell (Figure 12a).

If the morphology is analyzed, it can be observed that in zone one (Figure 12a), module 30 is more damaged than module 11. It is also observed that the thickness of the copper collector decreases in the event that thermal runaway has occurred, and it is observed to be narrower in the case of module 30.

Subsequently, the chemical composition of zone 1 (Figure 12a) is analyzed in the case of the cell of module 30 that caught fire (Figure 48).

Figure 48e shows the structure of the pouch cell of the burned module 30 in zone 1, four zones have been marked with a green box in which the composition of each of the layers of this pouch cell will be analyzed (Figure 48a–d).

Figure 48a identifies a compound of nickel and oxygen in zone 1 with traces of carbon and manganese, a compound of manganese and oxygen in zone 2, and a compound of carbon and oxygen in zone 3. Figure 48b identifies a compound of copper, carbon, and oxygen in zone 1 and zone 3; copper in zone 2, which is the anode collector; and a compound of carbon and oxygen in zone 4. Figure 48c identifies carbon, anode coating in zone 1, a compound of manganese, oxygen, and carbon in zone 2, cathode coating in zone 2, cathode aluminum collector in zone 3, fluorine from the electrolyte in zone 4, and a compound of aluminum and oxygen in zone 5. Finally, Figure 48d identifies a compound of copper, carbon, and oxygen in zones 1 and 3, copper in zone 2, which is the copper collector of the anode, and a compound of carbon and oxygen in zone 4.
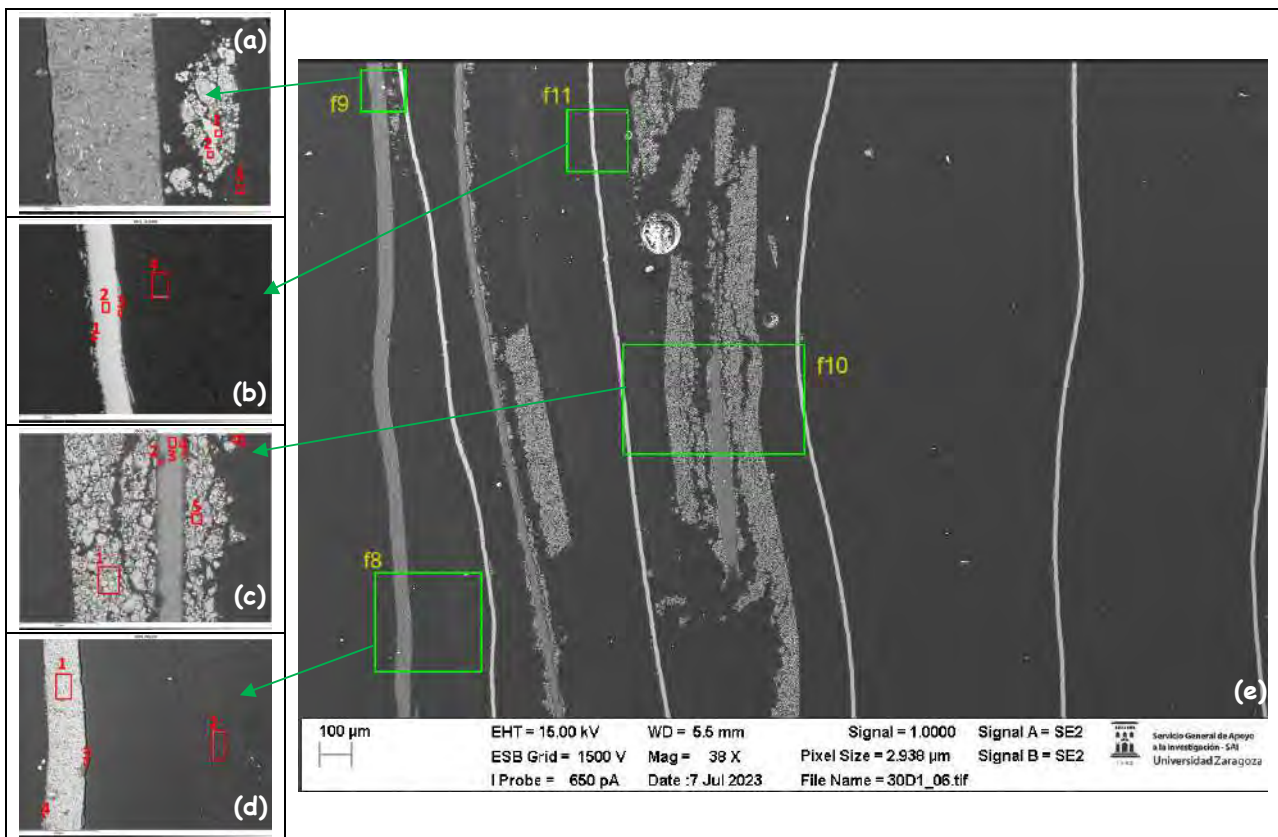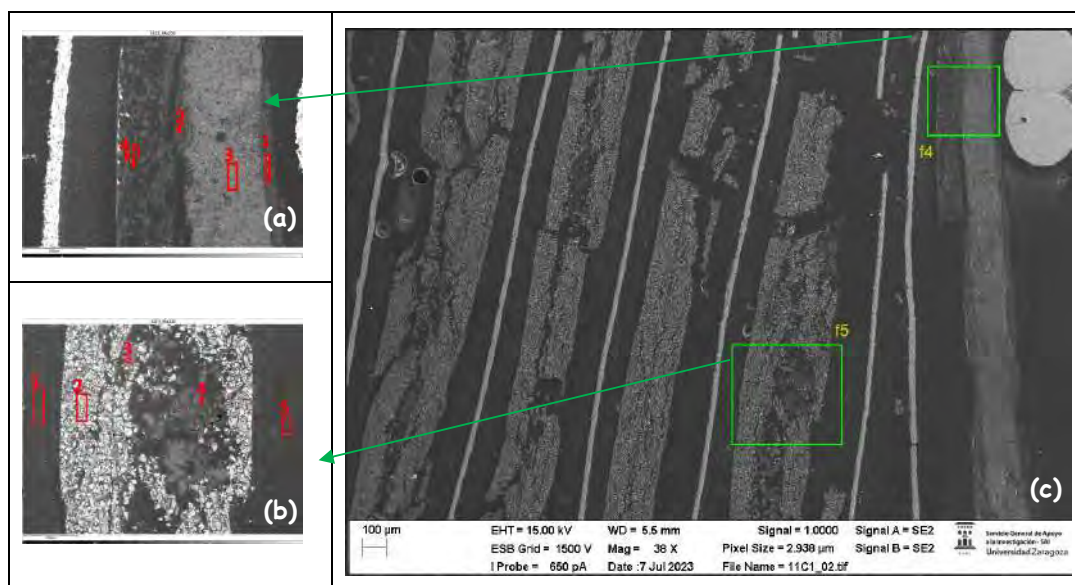
Figure 48. Chemical composition of each of the layers of the pouch cell of module 30 in zone 1 (anode zone) (Figure 12a).

Next, the chemical composition of zone 1 (Figure 12a) is analyzed in the case of the cell of the burned module 11.

Figure 49c shows the structure of the pouch cell of the burned module 11 in zone 1, two zones have been marked with a green box in which the composition of each of the layers of this pouch cell will be analyzed (Figure 49a,b).

Figure 49. Chemical composition of each of the layers of the pouch cell of module 11 in zone 1 (anode zone) (Figure 12a).

Figure 49a identifies a compound of carbon, oxygen, and aluminum in zones 1 and 2; aluminum and carbon in zone 3, which is the pouch bag; and in zone 4, there are carbon, oxygen, aluminum, and some copper. And in zone 5, there is carbon, which is the coating of the anode. In Figure 49b, a compound of carbon and oxygen is identified in zones 1, 4, and 5; in zone 4, there is also some aluminum. In zone 2, there is a compound of manganese, carbon, and oxygen cathode coating, and in the center, zone 3, there is a compound of aluminum and oxygen from the aluminum collector that has melted down and disappeared.

The chemical composition of zone 1 is then analyzed in the case of the new cell (Figure 50).

Figure 50e shows the structure of a new pouch cell in zone 1, four zones have been marked with a green box in which the composition of each of the layers of this pouch cell will be analysed (Figure 50a–d).

Figure 50a identifies a compound of carbon and oxygen in the three zones analyzed, and Figure 50b identifies a compound of carbon and oxygen in zones 1, 2, 5, and 6, a compound of manganese, carbon, oxygen, and fluoride in zone 3, and carbon and aluminum in zone 4. Figure 50c identifies the bag, which is aluminum in zone 3, coated on both sides by a compound of carbon and oxygen. Figure 50d identifies the copper collector of the anode in zone 4, which is coated by a compound of carbon and oxygen.
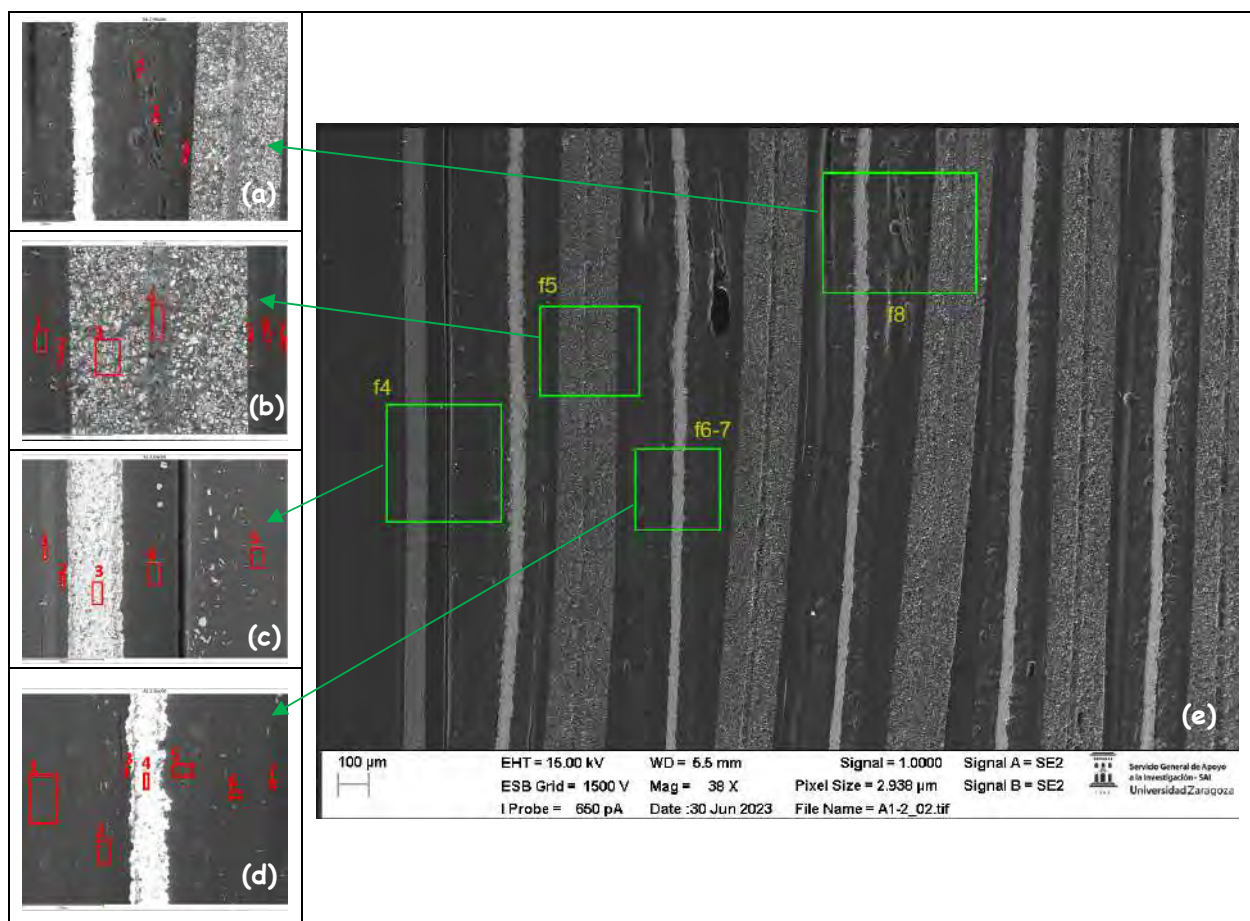

Figure 50. Chemical composition of each of the layers of the new pouch cell in zone 1 (anode zone).

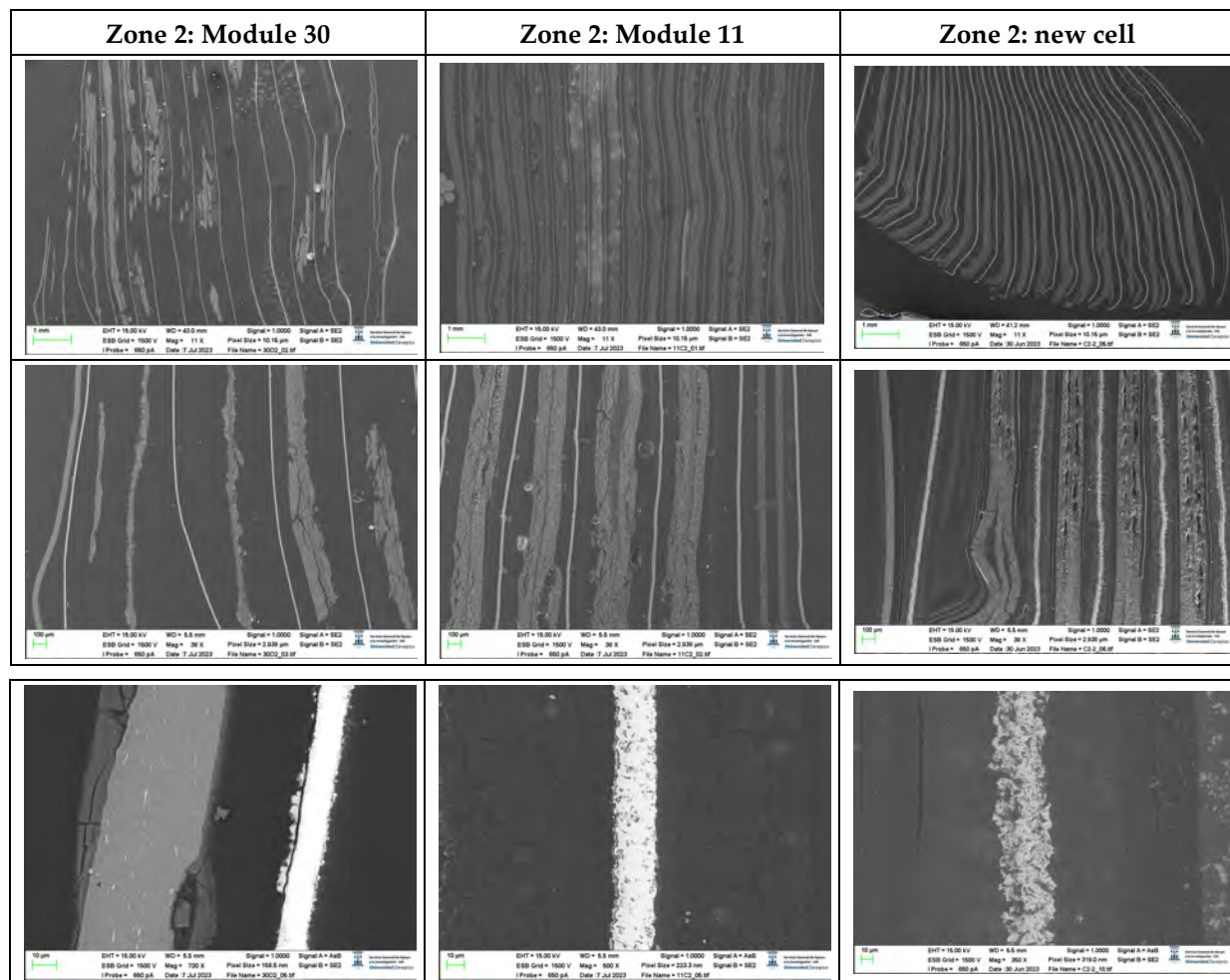The sample obtained in zone 2 (cathode battery tabs) is analyzed below (Figure 51):

Zone 2: Module 30	Zone 2: Module 11	Zone 2: new cell

Figure 51. Images of the pouch cell section in zone two (cathode zone) of the cell.

If the morphology is analyzed, module 30 is more damaged than module 11 in zone 2. It is also observed that the thickness of the copper collector decreases in the case of the cell experiencing thermal runaway, and it is observed to be narrower in the case of module 30.

Next, the chemical composition of zone 2 is analyzed in the case of the cell of the burning module 30 (Figure 52).

Figure 52d shows the structure of the module 30 pouch cell in zone 2, three zones have been marked with a green box in which the composition of each of the layers of this pouch cell will be analyzed (Figure 52a–c).

Figure 52a identifies a layer of a compound of carbon and oxygen (zone 1), a layer of a compound of aluminum and oxygen (zone 2) and the aluminum pouch (zone 3), a layer of an aluminum and oxygen compound (zone 5) and a layer of a carbon and oxygen compound (zone 6), anode copper collector (zone 8), and a layer of a compound of cooper and oxygen (zone 7 and zone 9). Figure 52b identifies a compound of manganese, carbon, and oxygen in zone 1 and 5, a layer of an aluminum and oxygen compound in zones 2 and 4, and aluminum and carbon in zone 3, the cathode collector. Figure 52c identifies a compound of copper, carbon, and oxygen in zones 1 and 3 and copper and carbon in zone 2, which is the collector and anode.
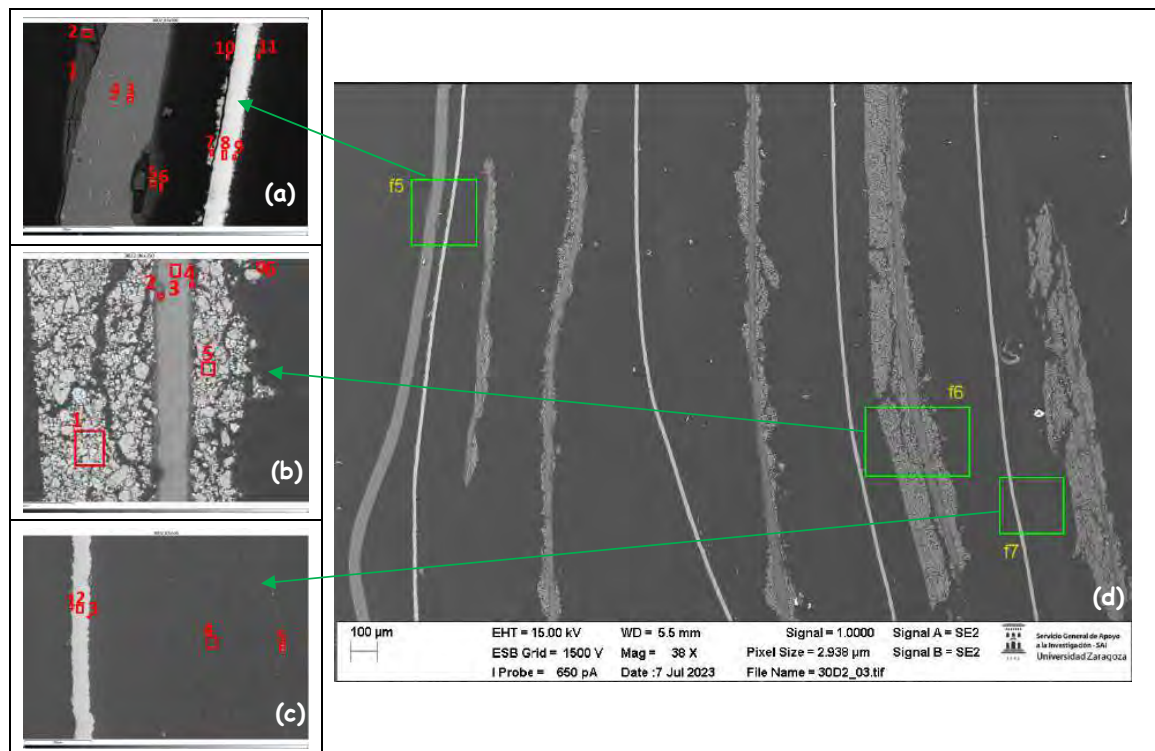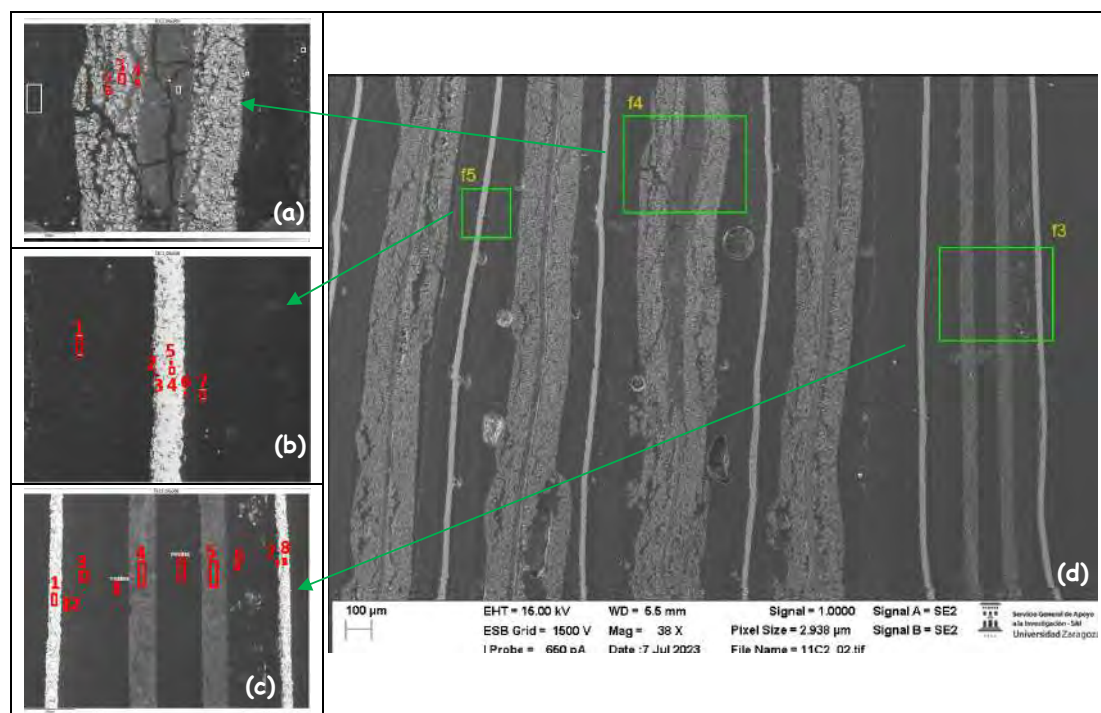
Figure 52. Chemical composition of each of the layers of the module 30 pouch cell in zone 2 (cathode zone).

Next, the chemical composition of zone 2 is analyzed in the case of the cell of the burning module 11 (Figure 53). Figure 53d shows the structure of the module 11 pouch cell in zone 2, three zones have been marked with a green box in which the composition of each of the layers of this pouch cell will be analyzed (Figure 53a–c).

Figure 53. Chemical composition of each of the layers of the module 11 pouch cell in zone 2 (cathode zone).

Figure 53a shows the cracking of the collector and cathode coating, identifying a compound of aluminum and oxygen (zone 2 and zone 4) within a layer of manganese, carbon, nickel, and oxygen (zone 3). Figure 53b identifies a layer of carbon (zone 1 and zone 7); a layer with a compound of copper, carbon, and oxygen (zones 2 and 3); a zone with a compound of copper and oxygen that is the collector of the anode; and a zone that has silicon (zone 5 and zone 6). Figure 53c shows a copper zone (zone 1 and zone 8) with two collectors; zones 4 and 5 are carbon and aluminum; resin layers are also identified; and in zone 7, carbon with traces of silicon and copper is observed. The silicon particles could be due to traces of a sealant material.

The chemical composition of zone 2 is then analyzed in the case of the new cell (Figure 54).

Figure 54d shows the structure of the new pouch cell in zone 2, three zones have been marked with a green box in which the composition of each of the layers of this pouch cell will be analyzed (Figure 54a–c).

Figure 54a shows the copper collector with carbon and some silicon (zone 4), a layer of a compound of carbon and oxygen on either side of the collector that comes from the graphite in the anode. Figure 54b shows the aluminum pouch with carbon and a compound of carbon and oxygen layers. Figure 54c shows layers of a carbon and oxygen compound, zone 3 shows aluminum and carbon, zone 4 shows a compound of manganese and oxygen, and zone 5 shows carbon and silicon. As stated above, the silicon particles could be due to traces of a sealant material.
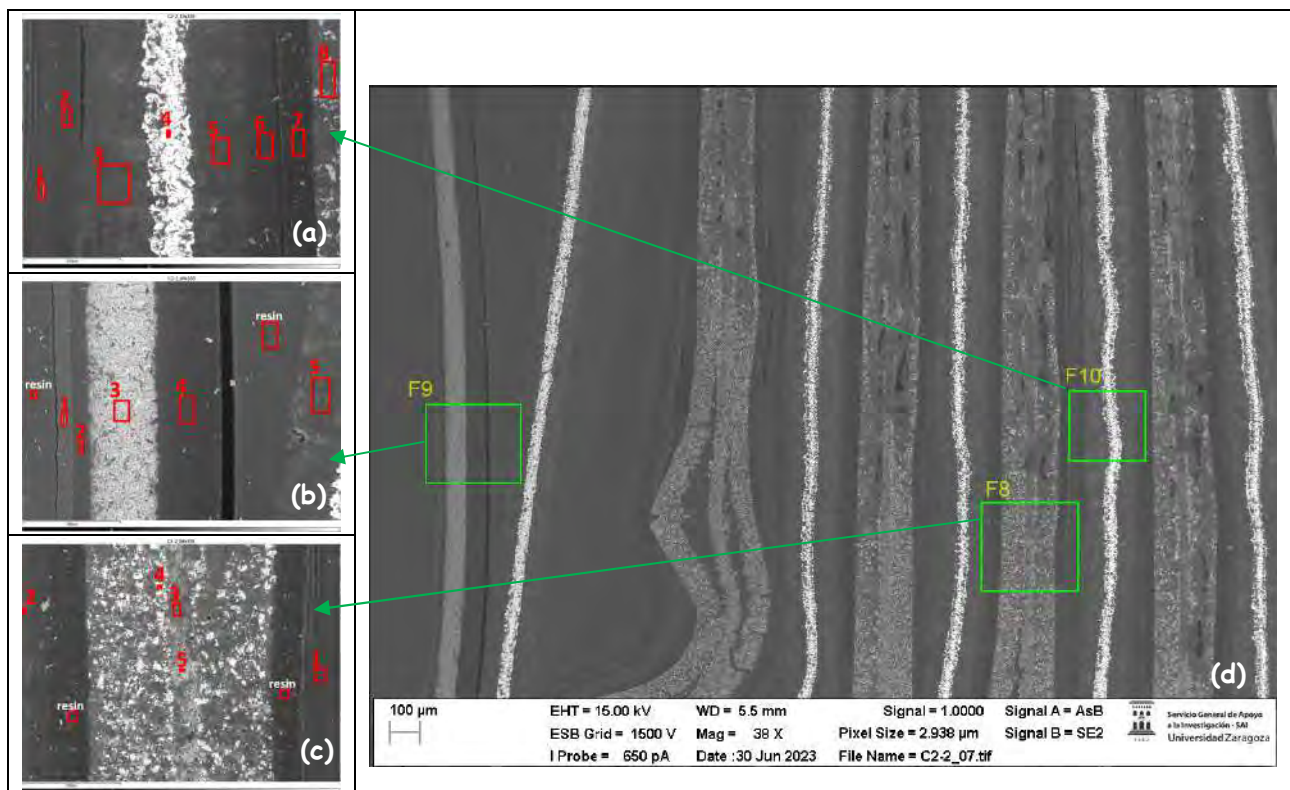

Figure 54. Chemical composition of each of the layers of the new pouch cell in zone 2 (cathode zone).

4. Conclusions

After analyzing the results obtained on the state of the cells subjected to thermal runaway in each of the analyzed arrangements, both vertical and horizontal arrangement, and compared with the state of a new cell, the following conclusions are reached:

- After thermal runaway, the cathode surface is covered with off-white floccules, fragment debris from cathode materials, ash from cathode material and separators, and

products of exothermal reactions and traces of anode graphite. It is observed that in the case of module 11, there are more dark-colored floccules than in the case of module 30, and there are more in the upper cathode than in the lower cathode. Therefore, it is concluded that module 11, in a vertical arrangement, experiences higher temperatures in the thermal runaway at the same SoC as module 30, which is in a horizontal arrangement.

- Regarding the morphology, it is observed that in the case of the lower cathode of module 30 (horizontal arrangement), the particles are smaller compared to the upper cathode of module 30. This may be due to the higher temperature since it is more exposed. In the case of module 11 (vertical arrangement), there is no difference between the particle size of the upper cathode and the lower cathode.
- It is observed that in the case of modules 30 and 11 with a SoC at 68% after thermal runaway, the pouch cell layered structure was destroyed, and adhesion of the particles dispersed outside the original layered structure occurred. The positive electrode material (cathode) reacted at high temperatures and decomposed. On the other hand, carbon particles from the anode (negative electrode) went into the cathode (positive electrode) structure through the damaged diaphragm.
- In the lower cathode of module 30, there are higher amounts of fluorine, aluminum, manganese, phosphorus, nickel, and cobalt than in the upper cathode.
- Regarding module 11, a higher amount of the aluminum and oxygen compound is observed. This may be because, in this case, the aluminum collector has been more damaged than in the case of module 30.
- The analysis of the cell anodes after the fire test shows that the anode has peaks of oxygen and peaks of carbon, which could indicate the formation of lithium carbonate (Li_2CO_3). Nevertheless, we have to note that the EDS data can only identify elemental composition and its weight/atomic percentage without offering insights into the chemical structure of components.
- After carrying out the comparative analysis of the different cathodes analyzed, it can be concluded that the cathodes of the ignited modules present compounds containing the elements of the cathode coating, but also present in some areas aluminum from the melting of the aluminum collector of the cathode and copper from the melting of the copper collector of the anode. There are also traces of fluorine from the electrolyte (LiPF6). Copper only appears on the lower cathode of module 11, yet more compounds appear, so it can be concluded that this is the most damaged cathode analyzed.
- It is observed that when the cell fails, the pressure caused by the swelling due to outgassing leaves visible fractures in the cathode.
- Analysis of the stacked layer samples allowed us to understand interesting aspects of the interior of the investigated battery, including in the tab area of the battery an additional separator layer, and it showed that on the edge of the battery, the separator and bag were welded together.
- When analyzing the structure, it is observed that in zone 3, the cell of module 11 on the outside and the cell of module 30 on the inside are more damaged.
- In both zone 1 (anode) and zone 2 (cathode), the cell of module 30 is more damaged than that of module 11 and in the case of zone 2.

The results of this study indicate that a more thorough structural analysis of the different layers of the cell (visualization of coatings deposited due to the exothermic reaction, study of the separator pore size, among other characteristics) should be carried out to improve the identification of the material composition of each layer. On the other hand, the technique for obtaining the test samples is also important so that no impurities contaminate the sample.

Regarding the safety of the battery, the results of this study will allow us to determine which arrangement and structure of the cells within the battery pack is safer against thermal runaway due to thermal failure. On the other hand, the identification of the chemical composition of each of the cell layers and the compounds generated as a residue

of a lithium-ion battery after a thermal abuse test is very useful for the intervention of first responders and for developing safe procedures to implement in response to accidents involving lithium-ion batteries.

References

1. Noh, H.J.; Youn, S.; Yoon, C.S.; Sun, Y.K. Comparison of the structural and electrochemical properties of layered Li[Ni$_x$Co$_y$Mn$_z$]O$_2$ (x = 1/3, 0.5, 0.6, 0.7, 0.8 and 0.85) cathode material for lithium-ion batteries. *J. Power Sources* **2013**, *233*, 121–130. [CrossRef]
2. Electrek 2018. Available online: https://electrek.co/2018/06/16/tesla-model-s-battery-fire-investigating/ (accessed on 28 November 2023).
3. Yahoo!News. 2019. Available online: https://sg.news.yahoo.com/tesla-car-catches-fire-hong-kong-parking-lot-050418281--finance.html?guccounter=1&guce_referrer=aHR0cHM6Ly93d3cuZ29vZ2xlLmNvbS88&guce_referrer_sig=AQAAAClpkmgR9urlu5KzzVB-y0uh0DW8ghCIrL9EdFrWSrIT8vBTETyCHsDA7mD5_1traEOgmIBOpuOZXf4YnfLD95g-yLPIlILgysRGQE48TSCJ4CdwpZKHvgTWfNP0r98GLV4CHFC9g-qRRZo2c0GcQPZZ3X4LK_4Y66TUg90JdNlN (accessed on 28 November 2023).
4. CNN Business. 2019. Available online: https://edition.cnn.com/2019/05/16/business/tesla-fire-battery-software-update/index.html#:~:text=Tesla%20is%20upgrading%20the%20battery,and%20improve%20their%20overall%20longevity (accessed on 28 November 2023).
5. Electrek. 2023. Available online: https://electrek.co/2023/04/27/tesla-fire-police-believed-battery-arson/ (accessed on 28 November 2023).
6. Carnewschina. 2023. Available online: https://carnewschina.com/2023/08/09/tesla-model-s-fire-in-sichuan/ (accessed on 28 November 2023).
7. Cbsnews. 2023. Available online: https://www.cbsnews.com/sacramento/news/tesla-spontaneously-catches-fire-in-rancho-cordova-high-end-vehicle-scrap-yard/ (accessed on 28 November 2023).
8. Sun, P.; Bisschop, R.; Niu, H.; Huang, X. A Review of Battery Fires in Electric Vehicles. *Fire Technol.* **2020**, *56*, 1361–1410. [CrossRef]
9. Balakrishnan, P.G.; Ramesh, R.; Kumar, T.P. Safety mechanisms in lithium-ion batteries. *J. Power Sources* **2006**, *155*, 401–414. [CrossRef]
10. Chen, M.; Yuen, R.; Wang, J. An experimental study about the effect of arrangement on the fire behaviors of lithium-ion batteries. *J. Therm. Anal. Calor* **2017**, *129*, 181–188. [CrossRef]
11. Feng, X.; Ouyang, M.; Liu, X.; Lu, L.; Xia, Y.; He, X. Thermal Runaway mechanism of lithium ion battery for electric vehicles: A review. *Energy Storage Mater.* **2018**, *10*, 246–267. [CrossRef]
12. Wang, H.; Lara-Curzio, E.; Rule, E.T.; Winchester, C.S. Mechanical abuse simulation and thermal runaway risks of large-format Li-ion batteries. *J. Power Sources* **2017**, *342*, 913–920. [CrossRef]
13. Huang, P.; Wang, Q.; Li, K.; Ping, P.; Sun, J. The combustion behavior of large scale lithium titanate battery. *Sci. Rep.* **2015**, *5*, 7788. [CrossRef] [PubMed]
14. Fu, Y.; Lu, S.; Li, K.; Liu, C.; Cheng, X.; Zhang, H. An experimental study on burning behaviors of 18650 lithium ion batteries using a cone calorimeter. *J. Power Sources* **2015**, *273*, 216–222. [CrossRef]
15. Chen, M.; Zhou, D.; Chen, X.; Zhang, W.; Liu, J.; Yuen, R.; Wang, J. Investigation on the Thermal Hazards of 18650 Lithium IonBatteries by Fire Calorimeter. *J. Therm. Anal. Calorim.* **2015**, *122*, 755–763. [CrossRef]
16. Feng, X.; Fang, M.; He, X.; Ouyang, M.; Lu, L.; Wang, H.; Zhang, M. TR features of large format prismatic lithium ion battery using extended volume accelerating rate calorimetry. *J. Power Sources* **2014**, *255*, 294–301. [CrossRef]
17. Roth, E.P.; Doughty, D.H. Thermal abuse performance of high-power 18650 Li-ion cells. *J. Power Sources* **2004**, *128*, 308–318. [CrossRef]
18. Wang, Q.; Sun, J.; Yao, X.; Chen, C. Thermal behavior of lithiated graphite with electrolyte in lithium-ion batteries. *J. Electrochem. Soc.* **2006**, *153*, A329–A333. [CrossRef]

19. Ma, S.; Jiang, M.; Tao, P.; Song, C.; Wu, J.; Wang, J.; Deng, T.; Shang, W. Temperature effect and thermal impact in lithium-ion batteries: A review. *Prog. Nat. Sci.* **2018**, *28*, 653–666. [CrossRef]

20. Zhang, S. Problems and their origins of Ni-rich layered oxide cathode materials. *Energy Storage Mater.* **2020**, *24*, 247–254. [CrossRef]

21. Peng, Y.; Yang, L.; Ju, X.; Liao, B.; Ye, K.; Li, L.; Cao, B.; Ni, Y. A comprehensive investigation on the thermal and toxic hazards of large format lithium-ion batteries with LiFePO₄ cathode. *J. Hazard. Mater.* **2020**, *381*, 120916. [CrossRef]

22. Wang, Q.; Ping, P.; Zhao, X.; Chu, G.; Sun, J.; Chen, C. Thermal Runaway Caused Fire and Explosion of Lithium Ion Battery. *J. Power Sources* **2012**, *208*, 210–224. [CrossRef]

23. Bai, F.; Chen, M.; Song, W.; Feng, Z.; Li, Y.; Ding, Y. Thermal management performances of PCM/water cooling-plate using for lithium-ion battery module based on non-uniform internal heat source. *Appl. Therm. Eng.* **2017**, *126*, 17–27. [CrossRef]

24. Garg, M.; Tanim, T.R.; Rahn, C.D.; Bryngelsson, H.; Legnedahl, N. Elevated temperature for life extension for lithium ion power cells. *Energy* **2018**, *159*, 716–723. [CrossRef]

25. Galushkin, N.E.; Yazvinskaya, N.N.; Galushkin, D.N. Mechanism of gases generation during lithium-ion batteries cycling. *J. Electrochem. Soc.* **2019**, *166*, A897–A908. [CrossRef]

26. Wang, G.; Kong, D.; Ping, P.; He, X.; Lv, H.; Zhao, H.; Hong, W. Modelingventing behavior of lithium-ion batteries during thermal runaway propa-gation by coupling CFD and thermal resistance network. *Appl. Energy* **2023**, *334*, 12066. [CrossRef]

27. Wang, Z.; Mao, N.; Jiang, F. Study on the effect of spacing on thermal runaway propagation for lithium-ion batteries. *J. Therm. Anal. Calorim.* **2020**, *140*, 2849–2863. [CrossRef]

28. Fang, J.; Cai, J.; He, X. Experimental study on the vertical thermal runaway propagation in cylindrical Lithium-ion batteries: Effects of spacing and state of charge. *Appl. Therm. Eng.* **2021**, *197*, 11739. [CrossRef]

29. Feng, X.; Sun, J.; Ouyang, M.; Wang, F.; He, X.; Lu, L.; Peng, H. Characterization of penetration induced thermal runaway propagation process within a large format lithium ion battery module. *J. Power Sources* **2015**, *275*, 261–273. [CrossRef]

30. Feng, X.; Lu, L.; Ouyang, M.; Li, J.; He, X. A 3D thermal runaway propagation model for a large format lithium ion battery module. *Energy* **2016**, *115*, 194–208. [CrossRef]

31. Lopez, C.F.; Jeevarajan, J.A.; Mukherjee, P.P. Experimental analysis of thermal runaway and propagation in lithium-ion battery modules. *J. Electrochem. Soc.* **2015**, *162*, A1905–A1915. [CrossRef]

32. Wilke, S.; Schweitzer, B.; Khateeb, S.; Al-Hallaj, S. Preventing thermal runaway propagation in lithium ion battery packs using a phase change composite material: An experimental study. *J. Power Sources* **2017**, *340*, 51–59. [CrossRef]

33. Lamb, J.; Orendorff, C.J.; Steele, L.A.M.; Spangler, S.W. Failure propagation in multi-cell lithium ion batteries. *J. Power Sources* **2015**, *283*, 517–523. [CrossRef]

34. Gao, S.; Feng, X.; Lu, L.; Kamyab, N.; Du, J.; Comsn, P.; White, R.E.; Ouyang, M. An experimental and analytical study of thermal runaway propagation in a large format lithium ion battery module with NMC pouch-cells in parallel. *Int. J. Heat Mass Transf.* **2019**, *135*, 93–103. [CrossRef]

35. Kovachev, G.; Schröttner, H.; Gstrein, G.; Aiello, L.; Hanzu, I.; Wilkening, H.M.R.; Foitzik, A.; Wellm, M.; Sinz, W.; Ellersdorfer, C. Analytical Disection of an Automotive Li-Ion Pouch Cell. *Batteries* **2019**, *5*, 67. [CrossRef]

36. Zhu, X.; Sun, Z.; Wang, Z.; Wang, H.; Lin, N.; Shan, C. Thermal runaway in commercial lithium-ion cells under overheating condition and the safety assessment method: Effects of SoCs, cathode materials and packaging forms. *J. Energy Storage* **2023**, *68*, 107768. [CrossRef]

37. Shin, H.; Lee, Y.K.; Lu, W. Structural degradation of graphite anode induced by dissolved manganese ions in lithium-ion batteries. *J. Power Sources* **2022**, *528*, 231223. [CrossRef]

38. Arora, P.; Zhang, Z. Battery Separators. *Chem. Rev.* **2004**, *104*, 4419–4462. [CrossRef] [PubMed]

39. Luo, M.J.; Guo, Y.Z.; Kang, J.Q. Ternary-material lithium-ion battery SOC estimation under various ambient temperature. *Ionics* **2018**, *24*, 1907–1917. [CrossRef]

40. Wang, J.L.; Wu, H.L.; Cui, Y.H. A new class of ternary compound for lithium-ion battery: From composite to solid solution Acs. *Appl. Mater. Interfaces* **2018**, *10*, 5125–5231. [CrossRef]

41. Xie, H.J.; Sun, J.; Li, J.G.; Zhou, T.; Wei, S.P.; Yi, Z.H. Lithium-Ion Battery Thermal Runaway Electro-Thermal Triggering. Method and Toxicity Analysis. *IOP Conf. Ser. Earth Environ. Sci.* **2021**, *701*, 012007. [CrossRef]

42. Finegan, D.P.; Scheel, M.; Robinson, J.B.; Tjaden, B.; Michiel, M.D.; Hinds, G.; Bretta, D.J.L.; Shearing, P.R. Investigating lithium-ion battery materials during overcharge-induced thermal runaway: An operando and multi-scale X-ray CT study†. *Phys. Chem. Chem. Phys.* **2016**, *18*, 30912–30919. [CrossRef]